Guiding of Tectonic Plate Motions by Transform Faults and Mid-Ocean Ridges

Petra Hatalova

Thesis submitted for the degree of
Master in Geophysics
60 credits

Department of Geosciences and Centre for Earth Evolution and Dynamics
Faculty of Mathematics and Natural Sciences

UNIVERSITY OF OSLO

August 2019

Guiding of Tectonic Plate Motions by Transform Faults and Mid-Ocean Ridges

Petra Hatalova

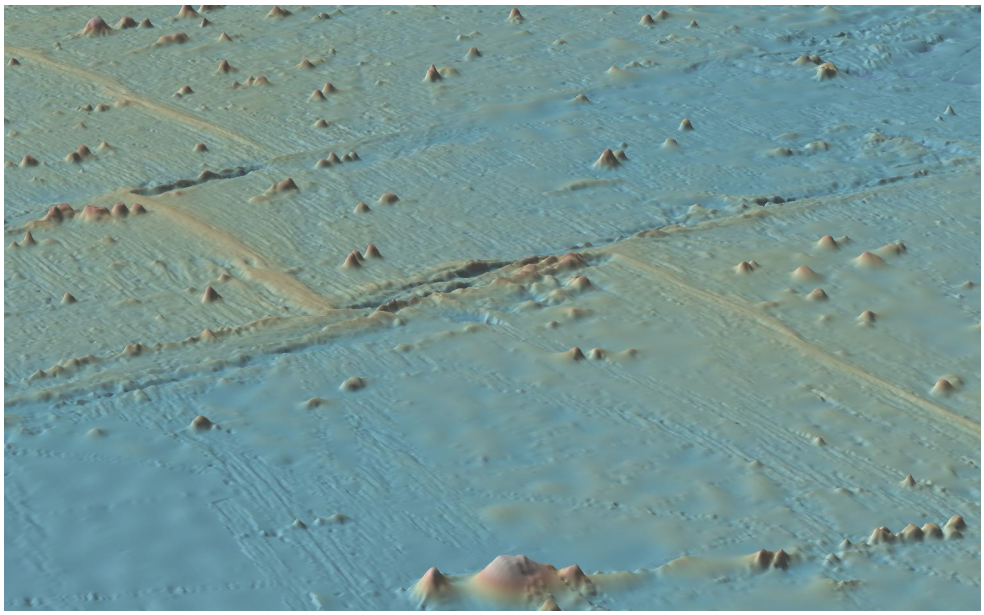

Guiding of Tectonic Plate Motions by Transform Faults and Mid-Ocean Ridges

Supervisor: Prof. Clinton P. Conrad

This work is published digitally through DUO

http://www.duo.uio.no/

Printed: Reprosentralen, University of Oslo

Cover figure: East Pacific Rise located close to Central America.

Acknowledgments

First of all, I would like to sincerely thank my supervisor Prof. Clint Conrad for his great support, absolute patience and all the constructive feedback. I would also like to thank my friends at the Master student room at CEED for all the fun and coffee, and my company Accenture for allowing me to take a long "holiday" to finish my studies.

In addition, I would like to thank my family and friends, especially the cows and my football teammates, for always being there for me.

Finally, I would like to thank D for making me stronger.

Abstract

Transform faults are strike-slip faults that accommodate lateral offsets between spreading segments of mid-ocean ridges. Because plates cannot move perpendicular to them, transform faults may exert a control on plate motions that has not been considered earlier. To improve some discrepancies between the predicted and observed plate motions, we introduce a force that resists plate motions parallel to mid-oceanic ridges (an alternative to a force perpendicular to the transform faults) into a larger-scale force balance that has previously been used to predict plate movements. Using three different misfit functions: misfit in direction, misfit in amplitude, and misfit in both direction and amplitude together, we constrain the magnitude of the new force, and compare its values to that of the major plate-driving forces. Our estimates of the ridge-parallel resistance expressed as a stress at plate boundaries are in a range between 16.5 and 44.0 MPa (assuming an average lithospheric thickness of 10 km at transform faults). The model previously used to predict plate motions is generally most improved when we use a value at the lower end of this range, but the improvement is typically minor. Our estimates of the actual force are between 0.8 and 2.1×10^{11} N/m, which is two orders of magnitude smaller than the expected value of the slab pull force, and one order of magnitude smaller than an estimate for ridge push. In general, even though the contribution of the ridge-parallel resistance to the force balance is relatively small, it slightly improves the predictions of the plate motions.

Contents

Chapter 1

Introduction

1.1 Aim of study

The theory of plate tectonics describes and predicts movements of lithospheric plates and explains why and how Earth's features are created. Some evidence suggests that on Earth this process started around 3 to 3.5 billion years ago (Van Kranendonk, 2011). Tectonic plates are either pushed towards each other at the convergent plate boundaries, or pulled away from each other at the divergent boundaries, or slide horizontally past each other. In the last case, we talk about transform plate boundaries or transform faults (also known as conservative plate boundaries). My Master's thesis focuses on the last one mentioned, specifically, on forces acting on plates at transform plate boundaries.

Most transform faults are strike-slip faults that accommodate lateral offsets between spreading segments of divergent boundaries, also called mid-ocean ridges. Figure 1.1 shows an example of a mid-ocean ridge interrupted by two transform faults. Movement at these boundaries is predominantly horizontal and it is believed that plates cannot move perpendicular to them, which means that transform faults may exert a control on plate motions that has not been considered earlier. A smaller number of transform faults connect mid-ocean ridges and subduction zones, which are convergent plate boundaries. One famous example of this case is the San Andreas Fault Zone of western North America, which connects a divergent boundary in the Gulf of California with the Cascadia subduction zone. The most prominent examples of the mid-oceanic ridge transform faults are in the Atlantic Ocean between South America and Africa, or along the East Pacific Ridge located in the South Eastern Pacific Ocean.

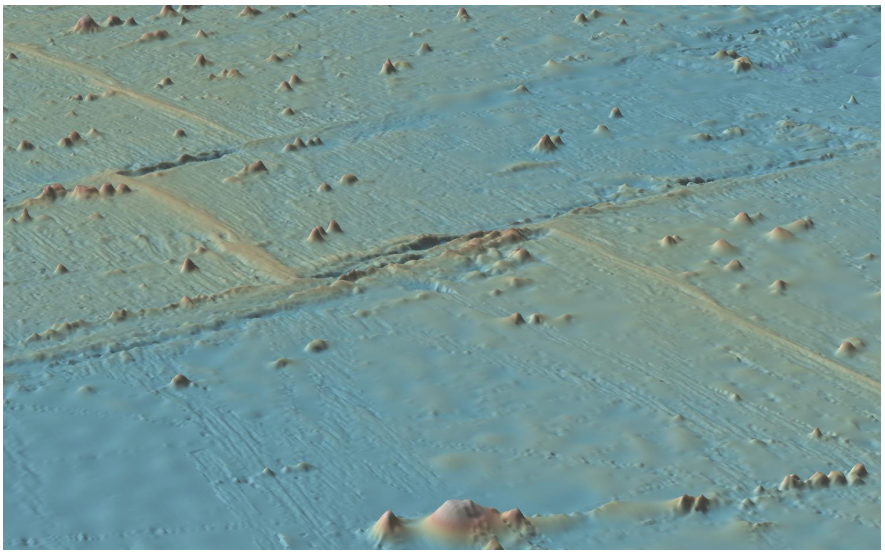

Figure 1.1: View of the East Pacific Rise mid-oceanic ridge (the straight line shown in warm colors) interrupted by transform faults perpendicular to the spreading center, located close to Central America. Image generated using the Global Multi-Resolution Topography (GMRT) Synthesis in GeoMapApp: http://www.geomapapp.org.

This project introduces a force that resists plate motions perpendicular to the transform faults (or, expressed alternatively, parallel to mid-oceanic ridges) into a larger-scale force balance that has previously been used to predict plate movements (e.g. Lithgow-Bertelloni and Richards, 1998; Conrad and Lithgow-Bertelloni, 2002, 2004). Presumably, there would be a large resistance to these perpendicular/parallel motions. Currently, in the plate motion prediction model, the plate is free to move across the transform faults, but this movement is not observed. Figure 1.2 presents this situation. The movement that is not observed is represented by the two red arrows. Therefore the force that we are introducing is acting in a direction opposite to those arrows. Inclusion of this force may help to explain some discrepancies between observed plate motions and those predicted by the force balance. The importance of transform faults remains an outstanding question in geodynamics.

1.2 Background information

Lithospheric plates are usually divided into major, minor, and micro plates. The seven major plates, which are larger than 20 million square kilometers, are the African plate,

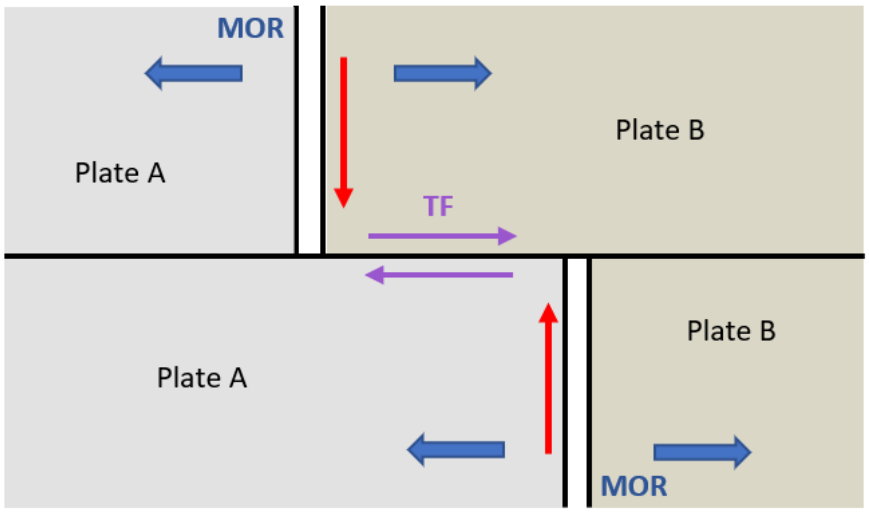

Figure 1.2: Simple sketch of plate motions at the plate boundary between plate A and plate B. The double vertical lines represent mid-oceanic ridges (MOR) and the horizontal line between them is a transform fault (TF). The blue arrows show the movement of plates at MOR and the purple ones the movements of plates at a TF. The red arrows represent the motion of tectonic plates in a perpendicular direction to the TF, which is not observed.

Antarctic plate, Eurasian plate, Indo-Australian plate, North American plate, Pacific plate and South American plate. In this project, we are using data for 12 plates: the seven major ones and five minor ones, which are the Arabian Plate, Caribbean Plate, Cocos Plate, Nazca Plate and Philippine Plate (see figure 1.3). Plates move at average rates of a few cm per year. The fastest moving plates are the Cocos and Pacific plates, which move at an average rate of 7.5 cm/year and 5.2-6.9 cm/year, respectively, and the slowest moving one is the Eurasian plate advancing at a speed of 2.1 cm/year (Kozák and Čermák, 2010).

One of the main questions of plate tectonics is what drives motion of the plates. Plate tectonics is an expression of the thermal state of the planet's interior. It is commonly accepted that the movement of the plates is fueled by thermal convection (see figure 1.4) taking place in the mantle, primarily by buoyancy forces caused by density heterogeneities associated with the convection (Turcotte and Oxburgh, 1967). The most important density heterogeneities in the mantle are actually parts of the oceanic plates descending into the mantle at subduction zones (McKenzie, 1969; Hager, 1984).

Plate tectonics is a complex dynamic system in which lithospheric plates interact with each other at the plate boundaries and with the mantle convection pattern in the as-

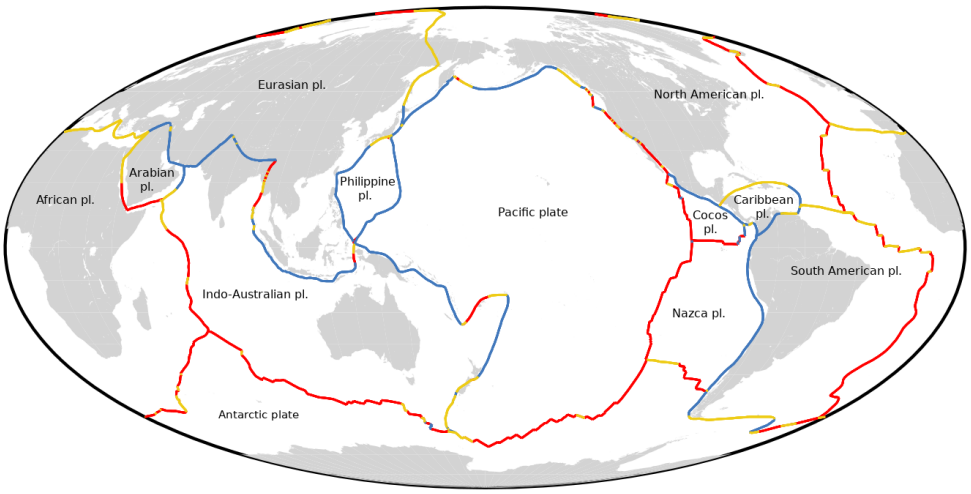

Figure 1.3: World map with continents in the background using the Mollweide projection, showing the 12 tectonic plates examined in my thesis and plate boundaries between them. Blue lines indicate convergent plate boundaries, red divergent boundaries and the yellow color shows locations of transform faults.

thenosphere (e.g. Tackley, 2000). Motion of a plate across the Earth's surface can be described by a defined pole of rotation (Euler pole) and the rate of the rotation around it. Determining the movements of individual plates relative to some common reference frame is not easy, but relative motions between pairs of plates can be determined quite easily. For example, the present-day plate motions, often called *geologically current*,

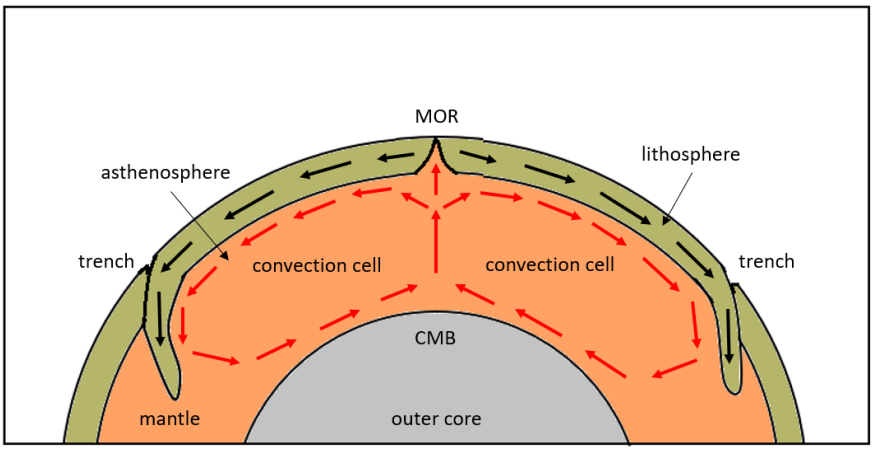

Figure 1.4: Thermal convection: hot material rises from the deepest part of the mantle to the asthenosphere, there it cools, sinks back and gets heated again. This cycle of heating, rising, cooling and sinking repeats over and over again and creates currents in the convection cells that are believed to drive the motion of tectonic plates. CMB means core-mantle boundary.

can be measured using the Global Positioning System (e.g. Argus and Heflin, 1995; Kreemer et al., 2003). Also, spreading rates along mid-ocean ridges can be established from magnetic anomaly patterns (e.g. Müller et al., 2008). In addition to the geologically current motions, those patterns can be used to reconstruct relative plate movements over geological time. This is possible due to reversals of the Earth's magnetic field that are preserved in linear bands of alternately polarized ocean crust.

Plate motions are controlled by gravitational forces within the mantle convection, such as **ridge push** (RP, see figure 1.5) at the spreading ridges (young hot plates are pushed away from ridges due to gravity acting down the slopes of a ridge) and **slab pull** (SP, see figure 1.5) in subduction zones (old cold and dense plates are pulled down towards these zones where they sink into the mantle). This downward pull associated with subducting slabs is believed to be the dominant force driving plate tectonics (Forsyth and Uyeda, 1975; Hager and O'Connell, 1981; Lithgow-Bertelloni and Richards, 1998). Comparatively, ridge push is not very important, as its net effect on the global force balance is small and represents only less than approximately 5-10% (Richter, 1975; Lithgow-Bertelloni and Richards, 1998; van Summeren et al., 2012). Figure 1.5 also presents **slab suction** (SS), which is caused by an induced mantle flow rather than by a slab directly pulling a subducting plate downwards. The difference between the slab pull and the suction will be explained in the next chapter. The fast velocities of the Cocos and Pacific plates, 7.5 cm/year and 5.2-6.9 cm/year, respectively (Kozák and Čermák, 2010), can be actually explained by those plates being oceanic plates with large lengths of subduction zones along their boundaries and slab pull being the main driving force acting on plates.

Apart from the driving forces, there are also resisting forces that are part of the system. They oppose the movements of the plates. **Slab resistance** (SR, see figure 1.5) occurs only at subduction zones, as the descending slab encounters resistance from the frictional drag on its upper and lower surface and from the viscosity of material that is being displaced. **Colliding resistance** (CR, see figure 1.5) is another resistive force caused by friction, which acts on both colliding plates that grind together at a subduction zone with equal magnitude and opposite direction. At transform boundaries, plates move past one another in opposite directions and this causes drag forces that resist this movement. This is called **transform fault resistance** (TR, see figure 1.2; this force is acting in the opposite directions than shown by the purple arrows that represent the movements of plates at a transform fault). Unlike other resistive forces,

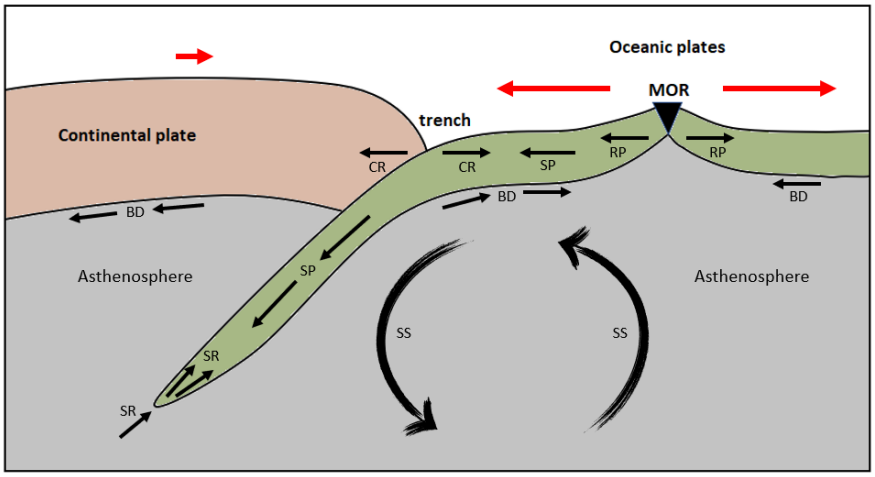

Figure 1.5: Driving and resisting forces acting upon tectonic plates (black arrows): slab pull (SP), ridge push (RP), slab resistance (SR), colliding resistance (CR), basal drag (BD) and slab suction (SS). The actual movement of the plates is indicated by the red arrows. The shorter red arrow signifies the lower speed of the overriding plate compared to the subducting one.

the **basal drag** (BD, see figure 1.5) force operates on almost all parts of a moving lithospheric plate. It is a frictional force acting at the interface between the base of a plate and the underlying asthenosphere. This drag force can actually act as a driving force as well. This happens when a lithospheric plate is being carried along by a faster moving asthenosphere.

These are the main forces resisting plate motions. In this thesis, we are trying to estimate the relative importance of another resistive force associated with mid-ocean ridges, the **ridge-parallel resistance**.

1.3 Goals of the project

The main goal of this project is to understand the influence of transform faults on global plate motions. Existing dynamically-driven plate models allow motions of plates perpendicular to these faults. We have adapted a numerical model to incorporate a force acting against these movements and evaluated the importance of this force compared to other forces acting on plates. Discrepancies between observed plate motions and the ones predicted by our numerical models are described, evaluated and explained if possible.

My Master's thesis has two deliverables. The first is the implementation of the ridge-parallel plate boundary force within an existing FORTRAN code (Lithgow-Bertelloni and Richards, 1998; Conrad and Lithgow-Bertelloni, 2002, 2004). The second is to investigate the influence of this force and its impact on associated plate motions. Both are described in detail in this document.

Chapter 2

Plate motions prediction

2.1 Previous findings

Tectonic plates are believed to be the surface expression of convection in Earth's mantle, driven primarily by the pull of subducting slabs and push from the spreading ridges, opposed by basal drag that resists plate motion at the interface between the lithosphere and upper mantle and colliding resistance at plate boundaries. This has been known already since 1970s from several independent studies that were based on either a process of trial and error or an inversion of plate velocities and the intraplate stress field in order to estimate the driving and resisting torques (Forsyth and Uyeda, 1975; Solomon et al., 1975; Chapple and Tullis, 1977; Gordon et al., 1978; Richardson et al., 1979; Richardson, 1992).

Plate forces associated with convective flows in the mantle predict plate movements consistent with the observed motions (Lithgow-Bertelloni and Richards, 1998), at least in terms of the direction of the movement. However, they often fail to reproduce the speed of oceanic plates correctly. The fast speed of oceanic plates relative to the continental ones suggests that an additional mechanism that can speed up those plates is required. According to the observations by Forsyth and Uyeda (1975), subducting plates move three to four times faster across the surface of the Earth than overriding plates. The pull of a sinking slab on a subducting plate via guiding stresses that are transmitted within the slab was proposed as a likely explanation (Elsasser, 1969), but the relative importance of this force on global patterns of plate motions had to be determined. Also, the exact mechanism by which the slabs drive plate motions is still being investigated.

Conrad and Lithgow-Bertelloni (2002) studied the effect of the slab weight as a one-sided edge force at plate boundaries and demonstrated that predicted plate motions agree best with observed motions when slab pull and mantle flow contribute approximately equally as driving forces. They also examined two possible ways of coupling the motions of slabs and plates: **slab suction**, when a detached slab sinking into the mantle induces mantle flow that exerts shear tractions at the base of the nearby plates, and **slab pull** when a slab remains attached to the rest of the subducting plate and transmits the downward pull directly to plate boundaries. Slab suction has been parameterized as a driving force for plates already by Lithgow-Bertelloni and Richards (1998) and Hager and O'Connell (1981), whereas slab pull was added by Conrad and Lithgow-Bertelloni (2002). In the last mentioned study, Conrad and Lithgow-Bertelloni have shown that the correct combination of these two mechanisms causes both subducting and overriding plates to move in the right direction at the right speed.

Inclusion of the ridge-parallel resistance may help to explain some of the still remaining discrepancies between observed plate motions and those predicted by the studies mentioned above (these discrepancies will be discussed briefly in the chapter 3). The importance of this force in the large-scale force balance has yet to be established.

2.2 Torque balance approach

The method used in this project to predict plate motions is the *torque balance approach* of Ricard and Vigny (1989) and Lithgow-Bertelloni and Richards (1998) updated by Conrad and Lithgow-Bertelloni (2002) by adding slab pull forces to the overall force balance. This approach was applied to compute sets of plate motions that are consistent with given combinations of slab pull and basal tractions on plates. These computed predicted plate velocities result from a balance between forces that drive and resist plate motions. It assumes a self-consistent set of plate motions and zero net torque on each plate (Solomon and Sleep, 1974), which means that tectonic plates are in mechanical equilibrium. The assumptions can be represented by a linearized system of equations or a torque balance (in plate tectonics, torque balance is used instead of force balance, since we are talking about rotating forces) between driving torques on the right side of the equation and resisting torques on the left side:

$$\mathbf{M}\,\vec{\omega} = \vec{Q} \tag{2.1}$$

In the equation 2.1, vector $\vec{Q}$ represents the driving torques, and thus it contains forces associated with slab pull and basal tractions from mantle flow exerted on plates. The method examines the torques on each plate, so there are 3 vector components for each of N tectonic plates, which makes it $3N$ elements of $\vec{Q}$ in total. In our case $N = 12$. Vector $\vec{\omega}$ is also a $3N$-dimensional vector that represents the respective Euler rotation vector for each of N tectonic plates in the system. Finally, $\mathbf{M}$ is a matrix with dimension $3N \times 3N$, which represents the resisting torques and depends on the viscosity and plate geometry. Diagonal elements of the matrix stand for viscous drag forces acting on a plate from the underlying mantle. All the other elements represent shear tractions that migration of one plate exerts on the neighboring plates via induced mantle flow. These tractions oppose the motion of the plates and can be calculated by rotating each plate a unit amount in each Cartesian direction, with the other plates held stationary. This is how the resistive torques are computed. Figure 2.1 presents the driving and resisting torques.

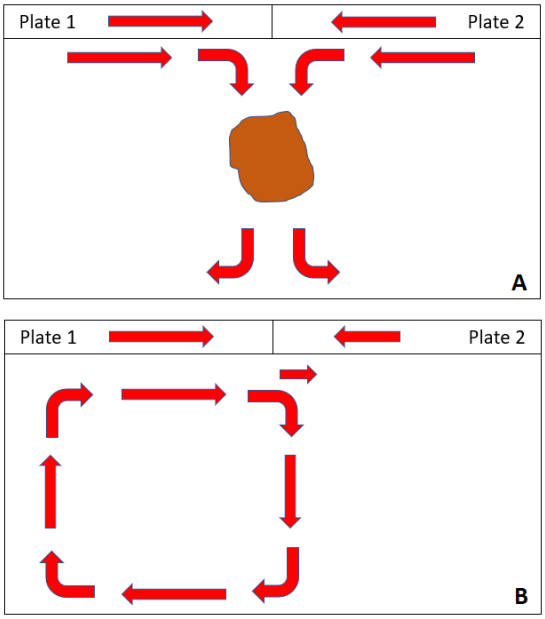

Figure 2.1: Simple sketch of driving and resisting torques acting on tectonic plates. Figure A represents driving torques $\vec{Q}_i$ and figure B resisting torques (that resist the movement of Plate 2) $\mathbf{M}_{ij}\vec{\omega}_j$.

The velocity vector $\vec{\omega}$ is computed as:

$$\vec{\omega}_j = \mathbf{M}_{ij}^{-1} \left(\vec{Q}_{int} + \vec{Q}_{pull} \right)_i \tag{2.2}$$

where $i, j = 1-3N$. The matrix representing the resisting torques needs to be inverted to $\mathbf{M}_{ij}^{-1}$. Vector $\vec{Q}_{int}$ contains applied torques due to internal density heterogeneities and $\vec{Q}_{pull}$ represents the slab pull force. The total driving torques for each plate is the vector sum of the torques from slab pull and tractions associated with mantle flow, which are integrated over the base of each plate.

Equation 2.2 needs to be solved for the motions of tectonic plates by first computing the driving torques and then finding such plate rotation poles that the resisting torques will exactly balance the driving torques. The fact that the resisting torques are linearly dependent on the rotation vector while the driving torques are completely independent, allows us to predict any $\vec{\omega}$. As the torque balance approach implies, driving torques and resisting torques must be in balance for each individual plate as well as for all plates in the system together. Plate motions are predicted by balancing the forces on each plate, and then applying the no-net-torque approximation to present the results in a no-net-rotation reference frame. For this method, plate motions are constrained up to an arbitrary net rotation of the lithosphere with respect to a stable lower mantle (Ricard and Vigny, 1989).

Eventually, a set of predicted relative plate motions in a no-net rotation reference frame is computed and can be compared to the observations. Figure 2.2 presents the observed surface plate velocities (following Conrad and Lithgow-Bertelloni (2004)), represented by the grey arrows, and the different types of plate boundaries: convergent, divergent and transform boundaries, distinguished by different colors. All of our predictions will be compared to this model of observed plate motions.

2.3 Limitations of the method

There are a few limitations of the *torque balance approach* as used e.g. in Lithgow-Bertelloni and Richards (1998) and Conrad and Lithgow-Bertelloni (2002, 2004).

Firstly, some assumptions had to be made: Newtonian rheology was chosen for mathematical convenience, and lateral viscosity variations, which may especially affect the movements of continental plates, were not allowed in the calculations. The effect of lateral viscosity variations associated with continental roots has been investigated by van Summeren et al. (2012). Even though their results suggest that continental roots may influence predicted plate motions, we are keeping our analysis simple to better estimate

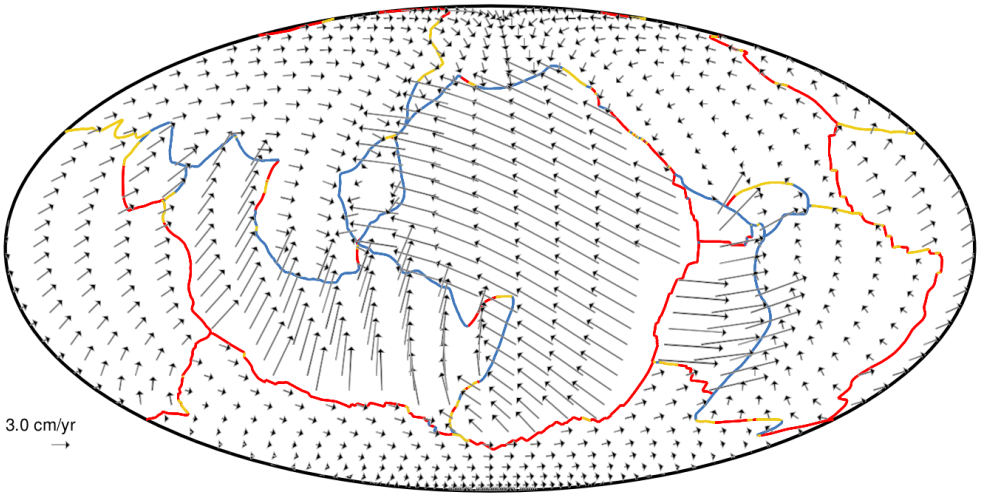

Figure 2.2: World map using the Mollweide projection. Observed plate velocities obtained from the observed poles of rotations, are represented by the grey arrows and different plate boundaries are shown in different colors. The blue color represents convergent plate boundaries, red divergent boundaries and yellow color shows locations of transform faults. The average observed velocity is 3.18 cm/yr.

the degree to which our force is important. In addition, some studies suggest that the lower mantle is complex with large variations in viscosity related to the composition of the rocks, which can have an impact on the buoyancy of the slabs in the uppermost lower mantle (Ballmer et al., 2015), but we have not included such variations in our calculations.

Generally, Earth's depth-dependent viscosity structure is uncertain. In this thesis, we use a viscosity structure from Conrad and Lithgow-Bertelloni (2004) that contains four layers with following values of viscosity:

radius in km (of the top of the layer)	**viscosity in 10^{21} Pa·s**	**layer**
6370.0	10.0	lithosphere
6240.0	1.0	asthenosphere
6140.0	1.0	transition zone
5700.0	50.0	transition zone

Plate velocities are directly proportional to viscosity, therefore assumptions about the viscosity profile should affect the results significantly. However, in order to not complicate the calculations, we have not considered the influence of different viscosity values.

Secondly, we use a slab model constructed based on the last 180 Myr of subduction by dropping slabs into the mantle beneath converging plate boundaries (Lithgow-Bertelloni and Richards, 1998). This slab history model contains only positive density anomalies and has been successfully used to reproduce plate motions by several authors, such as Conrad and Lithgow-Bertelloni (2002, 2004). Although, the model generally compares well with seismic and tomographic models, remaining differences might be improved by using more realistic dip angles for the subducting slabs (Lithgow-Bertelloni and Richards, 1998).

Thirdly, as well as viscosity, buoyancy forces are also uncertain. Only cold buoyancy (positive density) anomalies are considered, while active mantle upwellings are neglected. This may affect our calculations, even though it is believed that mantle plumes are responsible only for approximately 10% of the heat flux from the mantle (Davies, 1988; Sleep, 1990). However, large scale mantle flow may be more complex than previously expected. The possible plate-driving role of upwelling flow in the mantle has been examined by (Steiner and Conrad, 2007), and they concluded that active upwelling flows exhibit a similar pattern to downwelling flows.

Lastly, although the ridge push force has been included within the slab suction implementation (Lithgow-Bertelloni and Richards, 1998), several other forces that may contribute to the balance of forces acting on each plate have been ignored in the torque balance approach. The significance of these forces varies among plates. It may be important in driving or resisting motions of plates locally, but have not been shown to considerably improve fits to observed plate motions (Becker and O'Connell, 2001). These include forces associated with plate-plate interactions at different plate boundaries, e.g transform faults (e.g. Hall et al., 2003), continent-continent collisions (e.g. Richards and Lithgow-Bertelloni, 1996) or friction along plate-bounding faults at subduction zones (e.g. Conrad and Hager, 1999). Bending resistance is another possible resisting force that is not considered in this work, although its effect has been examined by Wu et al. (2008). Subducting slabs are cold and mechanically strong, therefore hinder the bending deformation that is necessary for plates to subduct and may significantly oppose plate motions (Conrad and Hager, 1999). Finally, compressive forces acting on subducting slabs may reduce the strength of the slab pull force for some subduction zones and therefore also act as resisting forces (Conrad et al., 2004).

Chapter 3

Our approach

3.1 Implementation of the ridge-parallel resistance

In this project, we are using the *torque balance approach* as described in the section 2.2 to predict plate motions. We have adapted the method to include the ridge-parallel resistance to constrain the relative importance of this force. The predicted motions are computed by utilizing the *midvel* code developed by Lithgow-Bertelloni and Richards (1998). The code was later updated to implement the slab-pull force by Conrad and Lithgow-Bertelloni (2002, 2004). This study uses the motions of the tectonic plates themselves as a constraint on the forces that drive them or oppose their movements. The predicted movements are then compared with plate motion observations in order to evaluate our results.

We examined a force that is perpendicular to the transform faults, but because we do not have a plate boundary resolution to identify all transform boundaries within the three types of boundaries (see section 3.3), we decided to focus on a force parallel to the mid-oceanic ridges instead, which is equivalent in terms of direction (as it is shown in figure 1.2). Mid-ocean ridges are generally much larger in length that transform faults, and are therefore easier to identify. That means that the new force that we have included in the *midvel* code is a force that opposes movements of the plates parallel to the divergent boundaries, and it is added only to the locations with this type of plate boundary. By adding this force to the force balance, we are trying to minimize this parallel motion.

After including our ridge-parallel resistance $\vec{Q}_{rpr}$ into the equation 2.2 representing the

torque balance, we get:

$$\vec{\omega}_j = \mathbf{M}_{ij}^{-1} \left(\vec{Q}_{int} + \vec{Q}_{pull} - \vec{Q}_{rpr} \right)_i \tag{3.1}$$

Vector $\vec{Q}$ now contains all previously considered driving torques and the new torque: $\vec{Q} = \vec{Q}_{int} + \vec{Q}_{pull} - \vec{Q}_{rpr}$. The expression for $\vec{Q}_{rpr}$ is introduced and explained below. Although our force is actually opposing the movement of the plates, we have implemented it into the part of the equation associated with driving forces for simplicity.

This final formula 3.1 needs to be solved for the motions of tectonic plates as described in the section 2.2. Firstly, we compute driving and resisting torques for each plate. Then the new torque $\vec{Q}_{rpr}$ is obtained and added to the equation. Next, we recalculate the driving and resisting torques for each plate (including $\vec{Q}_{rpr}$) and a new value of $\vec{Q}_{rpr}$ is obtained and added to the equation. We repeat the whole process until the calculated value of $\vec{Q}_{rpr}$ is not changing anymore. The equation needs to be solved iteratively, because we use plate velocities to calculate the ridge-parallel resistance and at the same time, plate velocities depend on the resistance. Finally, plate motions determined by the torque balance are compared to the observations. Based on this comparison, we are able to evaluate our predictions.

The process of obtaining the torque $\vec{Q}_{rpr}$ is described in the following steps:

1. We used a formula for slab pull force at a certain segment of a plate boundary from the *midvel* code (Lithgow-Bertelloni and Richards, 1998; Conrad and Lithgow-Bertelloni, 2002, 2004) and analogically wrote an equation for our ridge-parallel resistance:

$$\vec{F}_{rpr} = - \hat{s}_p \; L \; (FP_p - FP_o) \; D_{rpr} \tag{3.2}$$

   Here, $\hat{s}_p$ is a unit vector parallel to a segment (section between two adjacent points at a divergent plate boundary), since our force is acting in this direction. FP_p is a fraction of the parallel component of a velocity vector to the magnitude of the velocity for predicted plate motions (see the equation 3.3) and FP_o is this fraction for observed plate motions, L is the length of a segment (in m) and D_{rpr} is a scaling factor in N/m. We assume that the force is proportional to the difference between these two fractions $(FP_p - FP_o)$ and this factor scales the proportionality. The value of D_{rpr} needs to be estimated. The negative sign in the equation 3.2 represents the fact that the force resists ridge-parallel motion

and results in the positive value of D_{rpr}.

Equation 3.2 is the expression for our force $\vec{F}_{rpr}$ related to the torque $\vec{Q}_{rpr}$ from the equation 3.1. The negative sign for $\vec{Q}_{rpr}$ in that equation causes the torque to act in the right way on the average value of $(FP_p - FP_o)$, which is supposed to get smaller after each iteration.

The FP parameter was calculated using this formula:

$$FP = \frac{Vp_1 - Vp_2}{\left|\vec{V_1} - \vec{V_2}\right|} \tag{3.3}$$

In the equation 3.3, $\vec{V_1}$ and $\vec{V_2}$ are plate velocities of a plate 1 and 2 at the same point at a plate boundary, respectively, and Vp_1 and Vp_2 are components of velocities $\vec{V_1}$ and $\vec{V_2}$ parallel to the segment. The value of this FP parameter goes from -1 to +1 and determines how much movement at a plate boundary happens in a direction parallel to the considered segment. Figure 3.1 presents absolute values of the parameter at the plate boundaries around the world. Since we do not expect much of this movement at mid-oceanic ridges, FP values should be small there. In addition, if the used model already reproduces the observations well, then $(FP_p - FP_o)$ will be close to 0 and therefore the force (in equation 3.2) we add will be very small. The larger the difference at a mid-oceanic ridge, the larger value of our force is necessary to improve the predictions. All the information necessary to compute the force can be found in the data set we are using (Conrad and Lithgow-Bertelloni, 2004). Next, we needed to estimate the value of the scaling factor D_{rpr}.

2. The value of the factor was estimated to be in a range of 0 to 10^{13} N/m, where the highest limit is due to the slab pull estimates being around that value (e.g. Wu et al., 2008). We examined both positive and negative values of the factor and repeated the iterative process described above for each value to determine plate motions from the torque balance.

3. To evaluate the plate motion predictions for different values of D_{rpr}, we used a misfit function (see section 3.4).

4. After finding the best fit, the respective set of predicted plate motions was plotted

and compared to the observations (figure 2.2) visually.

3.2 Existing discrepancies

In this section, we will briefly discuss the discrepancies that still exist between observed plate motions and those predicted by the studies from Conrad and Lithgow-Bertelloni (2002, 2004). Their combination of upper mantle slab pull and lower mantle slab suction, provides the best predictions of observed plate movements so far (Wu et al., 2008). We expect these inconsistencies to be reduced by including our force to the overall force balance. Particularly, the inconsistencies associated with mid-oceanic ridges should be affected. The discrepancies are easily visible in figure 3.2, where the observed plate velocities are represented by the grey arrows and the predicted velocities by the purple arrows.

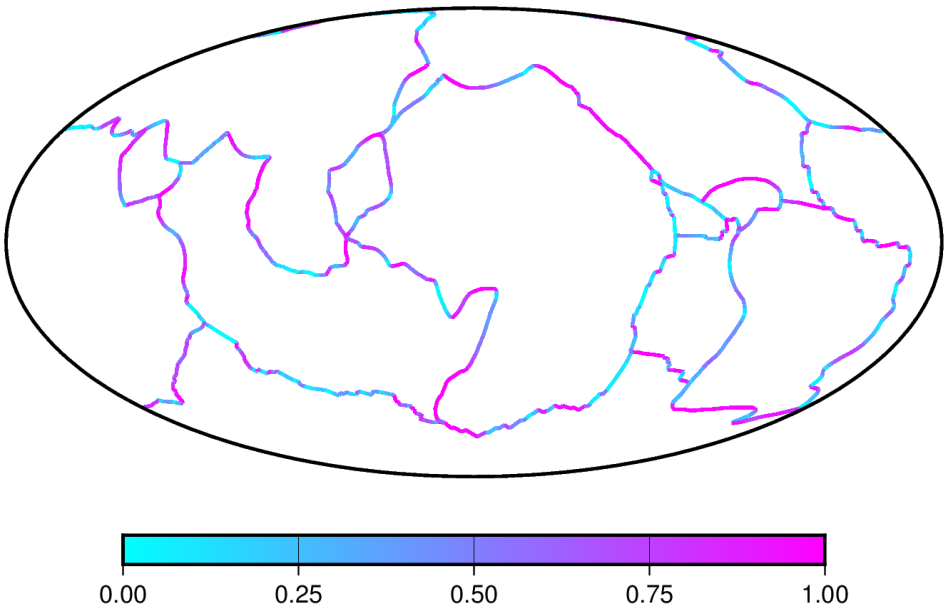

Figure 3.1: Map of values of the FP_o parameter at the plate boundaries around the world. FP_o is a fraction of parallel component of a plate velocity at a plate boundary to the magnitude of the velocity for observed plate velocities. Here we are using the absolute value of this fraction. Generally, the value should be close to 0 (blue color) at mid-oceanic ridges (e.g. the western boundary of the Nazca plate or the western and southern boundary of the Cocos plate) and close to 1 (purple color) at the transform faults (e.g. the northern and southern boundary of the South American plate). At subduction zones, the parameter should be also rather closer to 0 than to 1, but since oblique movement at these plate boundaries has been observed many times (e.g. Glazner, 1991), it does not need to be necessarily as close to 0 as for the ridges (e.g. the eastern boundary of the Nazca plate).

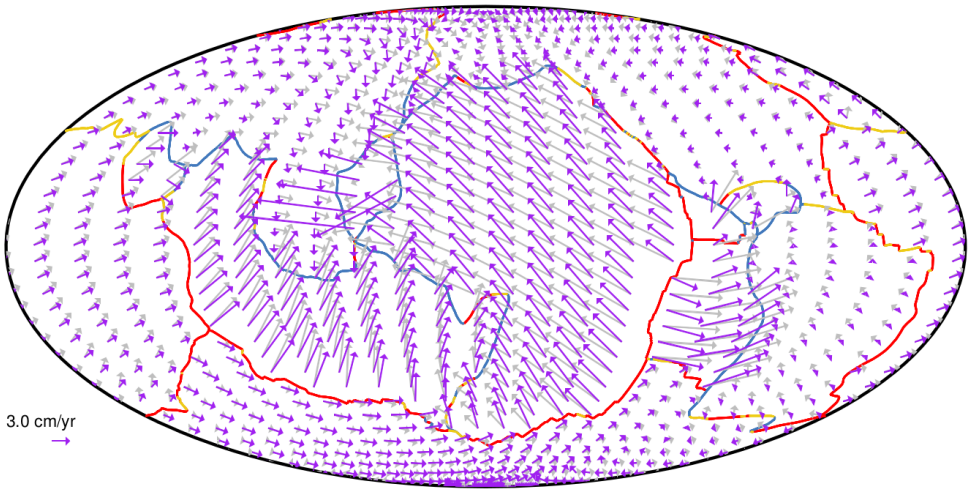

Figure 3.2: World map using the Mollweide projection, comparison of observed present-day plate motions (indicated by the grey arrows) with predicted plate motions (purple arrows) driven by a combination of direct slab pull from upper mantle slabs and slab suction from slabs in the lower mantle - figure made by using Conrad and Lithgow-Bertelloni (2002) model. The average predicted velocity is 2.79 cm/yr and the average observed velocity is 3.18 cm/yr.

We see that the predictions relatively closely match the observations in both the direction and the speed. The Philippine plate is an exception, the predicted movements are much faster than the observed ones, but this plate is surrounded by subduction zones, so we do not actually expect to improve the predictions for this plate. Besides, its motion is known to be complicated, since its parts move with quite different velocities (Smoczyk et al., 2010). Overall, the motions of the large plates are better reproduced than the motions of the small ones.

For our purposes, only the discrepancies related to mid-oceanic ridges/transform faults are interesting; these are what we are trying to minimize. For example, the direction and speed of the Pacific plate, Nazca and Cocos plate are expected to improve by adding the ridge-parallel resistance force to the force balance.

3.3 Plate boundaries identified

The new force has been added only to the segments of the plate boundaries that are classified as divergent plate boundaries. Therefore, before we include the new force to the force balance, the three types of plate boundaries had to be identified in our data set. For the identification of plate boundaries, we have used the definition of convergent

boundaries from the *subzone* code (Conrad and Lithgow-Bertelloni, 2004):

`if ((`V_{n1}`-`V_{n2}`) > 0.0) then we have convergence`

Here, V_{n1} is a component of a surface plate velocity perpendicular to a segment of a plate boundary, thus V_{n1} and V_{n2} are velocities (in cm/yr) of two plates (plate 1 and plate 2, respectively) normal to the same segment at a border between them. The negative sign for plate 2 reflects the fact that its segment is reversed. The V_{n1} is determined from:

$$V_{n1} = \vec{V_1} \cdot \hat{s}_n \tag{3.4}$$

In this formula, $\hat{s}_n$ is the normal to the segment and $\vec{V_1}$ is the actual surface plate velocity of plate 1 at a considered point of a plate boundary. V_{n2} can be calculated using the same equation.

Analogically, we have identified divergent boundaries:

`if ((`V_{n1}`-`V_{n2}`) < 0.0) then we have divergence`

Similarly, because the expected movement at transform faults is only parallel to the boundary, their definition should be:

`if ((`V_{n1}`-`V_{n2}`) = 0.0) then we have transform boundary`

Of course, this is not the case in the real physical conditions. Even at transform boundaries, plate motion will always have at least a small perpendicular component. Therefore, we had to establish a limit number (positive and negative) that separates the convergence and divergence and give some space to the transform faults. We have tried different values of the number from 0.1 to 2.0 (cm/yr) and compared the resulting map with a reference figure 3.3. The final definition (in cm/yr) of transform boundaries that we used is:

`if (-0.5` $\leq$ `(`V_{n1}`-`V_{n2}`)` $\leq$ `0.5) then we have transform boundary`

Using this value, we have managed to identify many of the known transform faults (see figure 2.2), but the resolution was still not good enough to identify a sufficient number of them for our purposes. This is the reason why we decided to focus on a force parallel to the mid-oceanic ridges instead. Consequently, the definitions of subduction zones and mid-ocean ridges used in this study are:

`if ((`V_{n1}`-`V_{n2}`) > +0.5) then we have convergence`

`if ((`V_{n1}`-`V_{n2}`) < -0.5) then we have divergence`

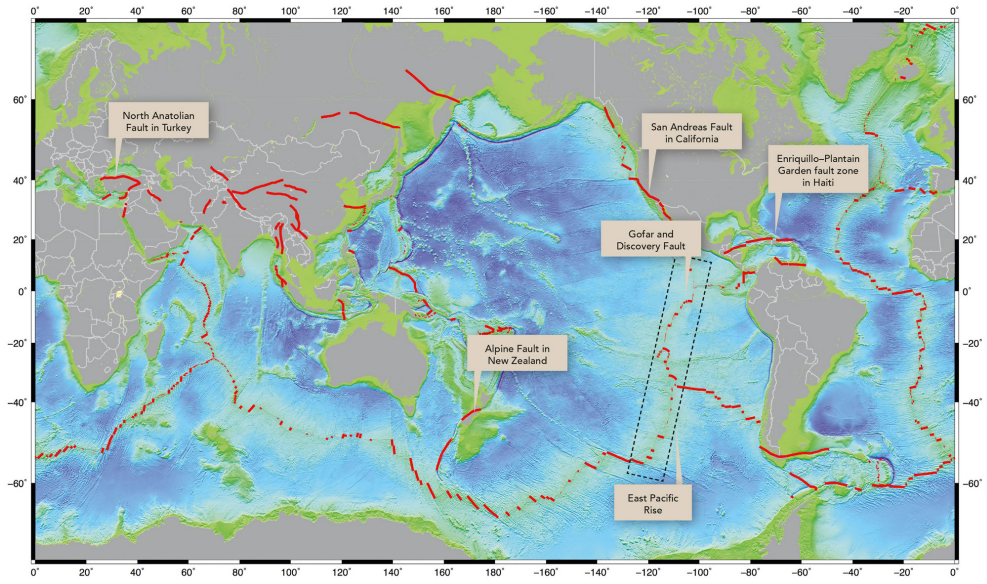

Figure 3.3: World map of transform faults, which are indicated by the red lines. Figure from an article by Wei (2017).

3.4 Plate motion diagnostics

In this section, I will explain how we compared our predictions of plate motions to the observations using a misfit function as a diagnostics, as used e.g. by Conrad et al. (2004) or van Summeren et al. (2012). Traditionally, the term *misfit* refers to the difference between measured data and predicted data. If the two values are sufficiently close, we consider the model to be a possible solution to our problem. In our case, the misfit function is the average magnitude of differences between vectors representing predicted and observed plate motions. The "perfect" fit would mean that both azimuths and amplitudes of predicted and observed velocities are matching perfectly at all locations. We have defined three different misfit functions: misfit in direction, misfit in amplitude, and misfit in both direction and amplitude together.

3.4.1 Misfit in direction

In this case, we examined only the directions of the vectors using

$$\phi_{d,i} = \frac{\vec{V_{pr}} \cdot \vec{V_{ob}}}{\left|\vec{V_{pr}}\right| \left|\vec{V_{ob}}\right|} \tag{3.5}$$

Equation 3.5 represents a misfit in direction for each pair of velocities, where observed plate velocities are $\vec{V_{ob}}$ and plate velocities predicted by our approach are $\vec{V_{pr}}$. The dot product in the numerator means that the best fit occurs if the value of the misfit is close to 1. At 1, the vectors representing observed and predicted velocities have the exactly same direction, whereas at -1, they have the exactly opposite direction. Therefore, the value of misfit varies in the range -1 to 1. To find the average value of the misfit for the whole Earth, we calculate the area-weighted average over the whole surface of the globe (equation 3.6), to take into account that the values of velocities in lower latitudes represent larger areas than the velocities close to the poles.

$$\phi_d = \frac{\sum\limits_i \phi_{d,i}\ A_i}{\sum\limits_i A_i} \tag{3.6}$$

Here A_i is a small area of size $A_i = \Delta lat\, \Delta lon\, \cos(lat)$, which is represented by a single surface velocity. In this equation Δlat is 5° and Δlon is 15°. Δ is a difference between two values of latitude or longitude in our data set.

3.4.2 Misfit in amplitude

Misfit in amplitude considers only the differences in the magnitudes of vectors:

$$\phi_{a,i} = \frac{\left|\vec{V_{pr}}\right| - \left|\vec{V_{ob}}\right|}{\left|\vec{V_{pr}}\right| + \left|\vec{V_{ob}}\right|} \tag{3.7}$$

In this case, the best fit is achieved when the value of misfit is close to 0, because the value of the numerator is 0 when the two vectors have the exact same magnitude. The value varies in the range -1 to 1.

3.4.3 Misfit in both direction and amplitude

Lastly, we examined both directions and magnitudes of the vectors simultaneously:

$$\phi_{da,i} = \frac{\left|\dfrac{\vec{V_{pr}}}{\langle V_{pr}\rangle} - \dfrac{\vec{V_{ob}}}{\langle V_{ob}\rangle}\right|}{\left|\dfrac{\vec{V_{pr}}}{\langle V_{pr}\rangle}\right| + \left|\dfrac{\vec{V_{ob}}}{\langle V_{ob}\rangle}\right|} \tag{3.8}$$

Here $\langle V_{ob} \rangle$ is the average observed velocity and $\langle V_{pr} \rangle$ the average predicted velocity. The value of misfit now varies from 0 to 1 and the best fit is close to 0. Equation 3.9 calculates the average plate velocity weighted by latitude for $\langle V_{ob} \rangle$. The same equation can be used to compute the average predicted velocity $\langle V_{pr} \rangle$.

$$\langle V_{ob} \rangle = \frac{\sum_i V_{ob,i} \cos(lat)}{\sum_i \cos(lat)} \tag{3.9}$$

For all three defined misfit functions, we calculate the area-weighted average over the whole surface of the globe using the equation 3.6. In addition, we compute the functions for the plate boundaries only, in which case we use velocities parallel and perpendicular to the boundaries and calculate the weighted average over the segments of the boundaries. Now the equation 3.6 will change to:

$$\phi_d = \frac{\sum_i \phi_{d,i} \, L_i}{\sum_i L_i} \tag{3.10}$$

L_i is the length of a segment.

Chapter 4

Evaluation of the results

4.1 Execution of the program

The program is executed in three different ways. Surface plate motions are either imposed (not solved for using a force balance) or determined by balancing torques due to both pull from upper mantle slabs and suction from lower mantle slabs and unconnected upper mantle slab material. In addition, we execute the second model also with our ridge-parallel resistance included, as described in section 3.1. The first case provides us with the observed velocities of the plates (figure 2.2). Output of the second case are the predicted velocities based on the torque balance method, specifically, predicted by the studies by Conrad and Lithgow-Bertelloni (2002, 2004). This is our reference model that we are trying to improve upon in this thesis. By comparing these two outcomes, we can evaluate the reference model and focus on the discrepancies between the model and the observations as we did in section 3.2. At last, but most importantly, we run the program including the ridge-parallel resistance and compare the results to the reference model and to the observations as well. For this evaluation, we apply the various misfit functions defined in section 3.4.

In this chapter, I present and evaluate our key findings by examining the three defined misfit functions, the resulting patterns of predicted plate velocities compared to the observations, and subtraction plots of the two outputs mentioned above, to show if and where our models improve the existing predictions. In addition, I provide maps showing the magnitude of the ridge-parallel resistance at the plate boundaries for each of our models. Our final estimate of the ridge-parallel resistance is expressed in N/m and also as a stress in Pa (our force in N/m divided by an average thickness of the

lithosphere). To calculate the stress, we assume an average lithospheric thickness of 10 km at transform faults, where the force usually has the maximum effect due to typically shorter lengths along the transform faults. The results are divided into separated sections according to the misfit function used.

4.2 Results evaluated by misfit in direction

4.2.1 Misfit in direction (whole Earth)

To find the best fit for this misfit function, we varied the scaling factor D_{rpr} between 0 and 10^{13} N/m in equation 3.2, and then evaluated the results of the torque balance using equations 3.5 and 3.6. In this case the best fit occurs when the misfit value is closest to 1. As described in section 3.1, we obtain the best value of D_{rpr} by solving equation 3.1 iteratively. To investigate the impact of the iterations on our best fit, we inspect figure 4.1, which displays the misfit in direction over the whole surface of the globe calculated with and without the iterations. The red dashed line is a result of execution of the code with 5 iterations and the blue one is without any iterations (the code was executed only once). The best fit for each function is indicated by the red and blue circles, respectively. From the graph, it is obvious that the iterations do not actually improve the fit. They help only in a small range of values (where the red dashed line is above the blue line) where there is a big difference in observed and predicted velocities, but do not improve the best fit. Because of this we decided to omit the iterations, since running the code iteratively is much more time-consuming.

Figure 4.2 presents the misfit in direction again, this time comparing the best fit to the misfit for a zero value of the scaling factor D_{rpr} to show the effect of including the ridge-parallel resistance in the torque balance. When $D_{rpr} = 0$ N/m, then the ridge-parallel resistance is zero as well. The best fit of 0.8387 was computed for a value of 6.28×10^{11} N/m of D_{rpr} (the pink circle on the right). The misfit for a zero value of the scaling factor is 0.8313 and is marked with the pink circle on the left. We see that the best fit was only slightly improved after adding the ridge-parallel resistance in this case. Using this value of the factor (6.28×10^{11} N/m), the average magnitude of the ridge-parallel resistance expressed as a stress is calculated to 22.0 MPa (assuming an average lithospheric thickness of 10 km at transform faults). To obtain this value of the stress, we used the force from equation 3.2 where the difference $(FP_p - FP_o)$ is a

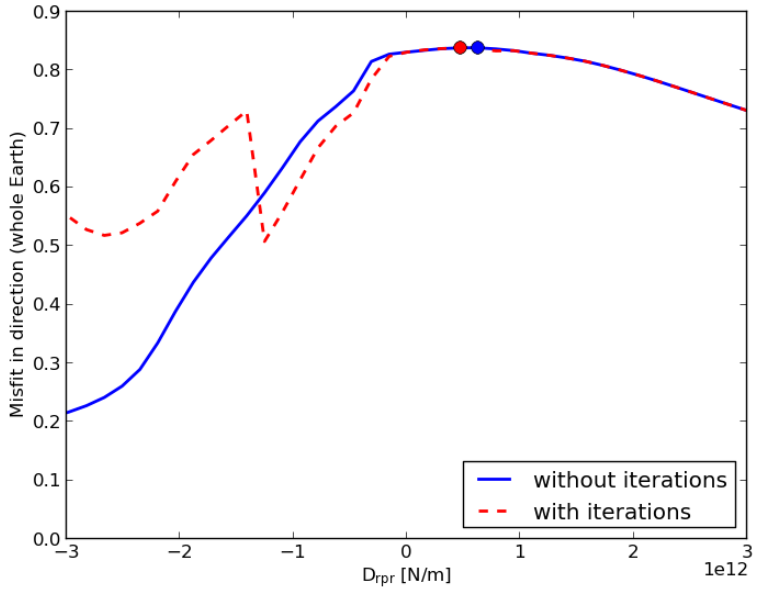

Figure 4.1: Misfit in direction over the whole surface of the globe calculated with and without iterations. The red dashed line represents the function computed with 5 iterations and the blue one is without iterations. The best fit for each function is indicated by the red circle (with iterations) and blue circle (without iterations). The best value of the scaling factor D_{rpr} was found to be 6.28×10^{11} N/m with the best misfit of 0.8387 from the calculations without the iterations and 4.71×10^{11} N/m with the best misfit of 0.8382 from the calculations with the iterations.

number with values from -2 to +2 and an average value of 0.35. So, the average stress equals the scaling factor times the average difference divided by the average thickness.

The next figure 4.3 presents a subtraction of the misfits (in absolute value) for the best value and zero value of the scaling factor for the velocities on the whole globe. This map clearly shows areas where adding our force improves the predictions of the previously used model Conrad and Lithgow-Bertelloni (2002, 2004), indicated by the blue color, and areas where adding our force actually make the predictions worse (the red areas). The improved areas are parts of the Arabian, Cocos, Caribbean and Antarctic plates. Slightly blue are also Pacific, Philippine, Eurasian and African plates. The rest shows no improvement or predictions even worsen, like e.g. both North and South American plates. Parts of the two of the small plates (Arabian plate and Caribbean plate) experience significant worsening. Similar patterns of improvements and worsening can be found by comparing figure 3.2, showing the predictions of the previously used model Conrad and Lithgow-Bertelloni (2002, 2004), with figure 4.4.

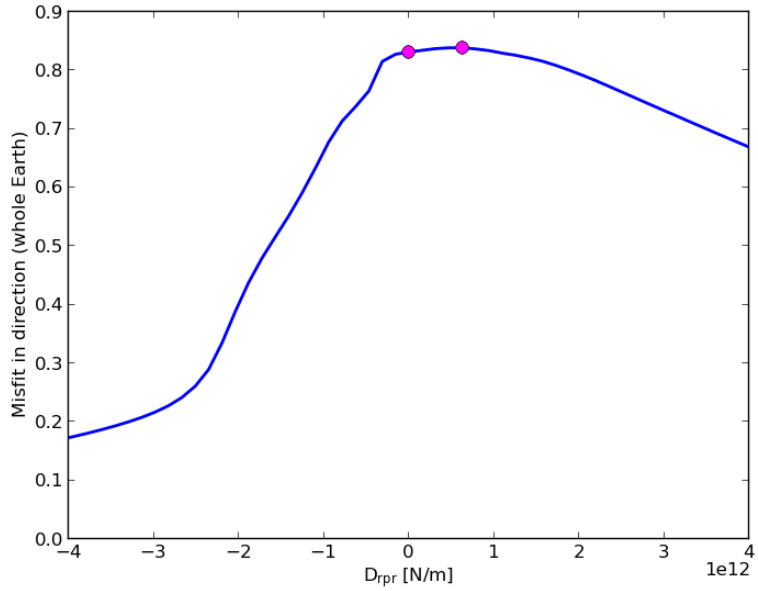

Figure 4.2: Misfit in direction over the whole surface of the globe. The best fit of 0.8387 for $D_{rpr} = 6.28 \times 10^{11}\ N/m$ and the misfit 0.8313 for a zero value of the scaling factor are marked with the pink circles.

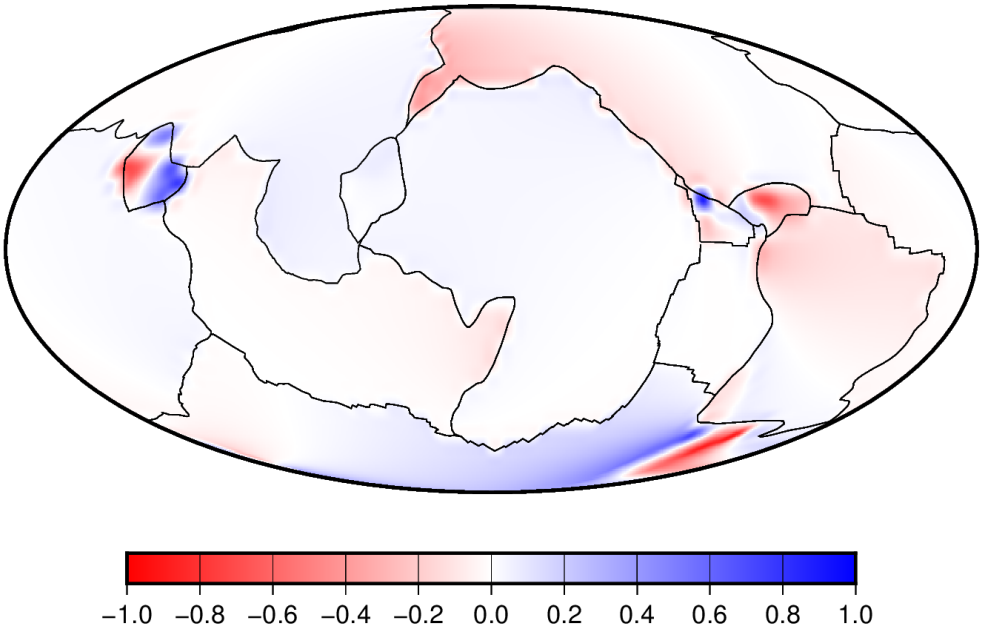

Figure 4.3: Subtraction plot of the misfits (in absolute value) for the best value $D_{rpr} = 6.28 \times 10^{11}\ N/m$ and zero value of the scaling factor for the velocities on the whole globe. The blue color indicates the areas where adding our force improves the previously used model, the red areas represent regions where the predictions are getting worse after adding the ridge-parallel resistance.

Finally, figure 4.4 shows predicted plate velocities compared to the observations using the best value of the scaling factor $6.28 \times 10^{11}\ N/m$. Here and in all the maps with the predicted plate velocities in this study, we are using the observed plate velocities to identify the different types of plate boundaries, not the predicted ones, to be able to compare the actual predictions to the observations.

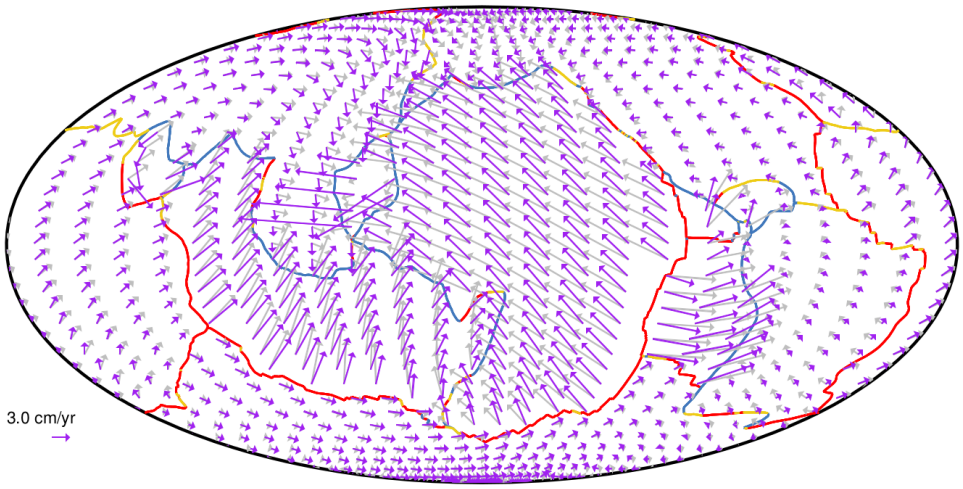

Figure 4.4: World map using the Mollweide projection, comparison of observed present-day plate motions (indicated by the grey arrows) with predicted plate motions (purple arrows) for $D_{rpr} = 6.28 \times 10^{11}\ N/m$. The average plate velocity for this model is 2.84 cm/yr.

At the end of this section, I include a global map of a magnitude of the ridge-parallel resistance calculated from equation 3.2 and added to the torque balance (see figure 4.5). We see that the resistance is displayed only at mid-ocean ridges where it was added. The highest values are associated with the Pacific plate, particularly with its east plate boundary, which is the East Pacific Rise. The northern and southern parts of the East Pacific Rise belong among the fastest spreading ridges in the world, which agrees very well with the pattern on this map. On the other hand, the weakest force is displayed around African plate and this is where the slowest spreading ridges can actually be found.

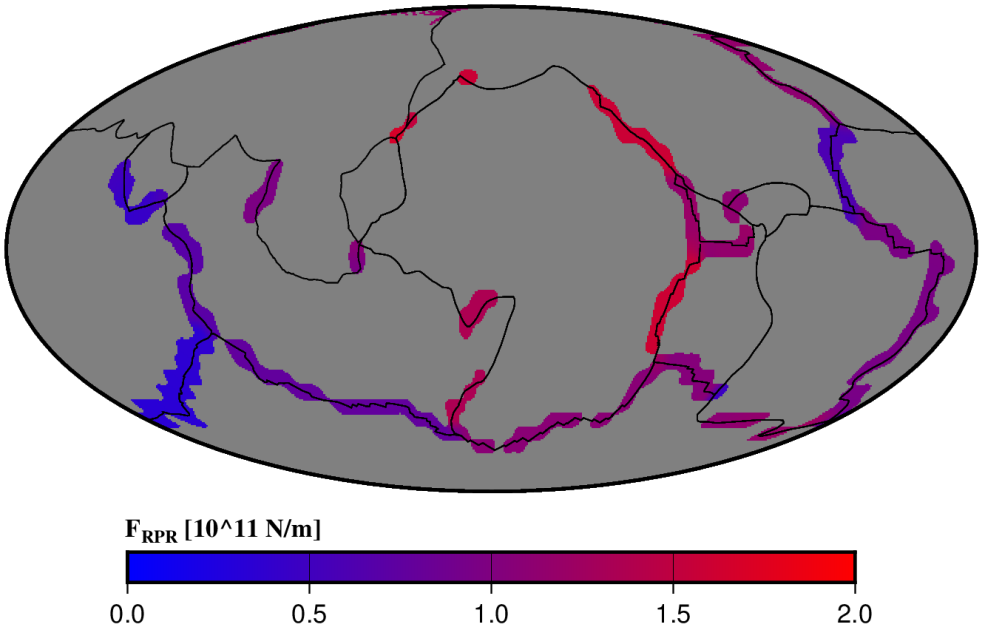

Figure 4.5: World map of a magnitude of the ridge-parallel resistance added to the torque balance at the mid-ocean ridges for $D_{rpr} = 6.28 \times 10^{11}\ N/m$.

4.2.2 Misfit in direction (plate boundaries)

Figure 4.6 presents the misfit in direction at the plate boundaries. We again compare the best fit to the misfit for a zero value of the scaling factor D_{rpr}. The best fit of 0.7576 was computed for a value of $4.71 \times 10^{11}\ N/m$ of D_{rpr} (the pink circle on the right). The misfit for a zero value of the scaling factor is 0.7160 (the pink circle on the left). In this case, the best fit was more improved after adding the ridge-parallel resistance than in the previous case for the whole Earth. Using this value of the factor, the average magnitude of the ridge-parallel resistance expressed as a stress at a certain segment of a plate boundary was calculated to 16.5 MPa (assuming an average lithospheric thickness of 10 km at transform faults).

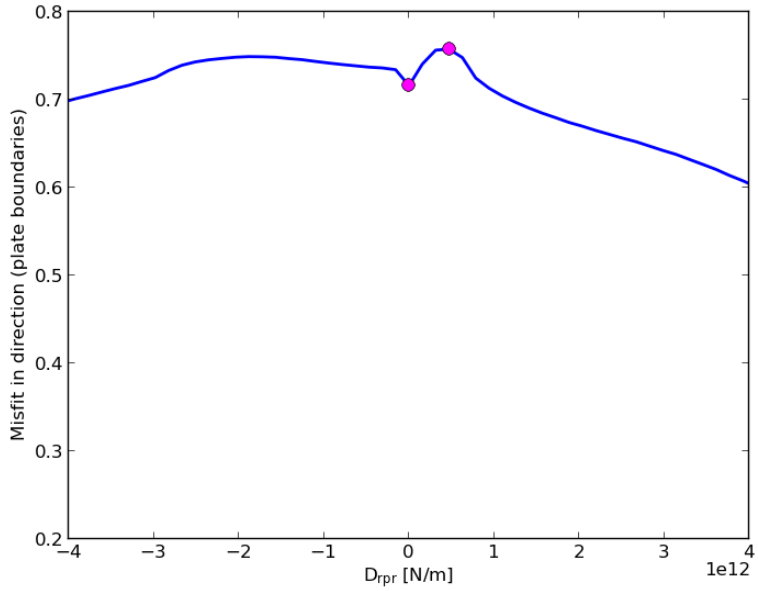

Figure 4.6: Misfit in direction at the plate boundaries. The best fit of 0.7576 for $D_{rpr} = 4.71 \times 10^{11}\ N/m$ and the misfit 0.7160 for a zero value of the scaling factor are marked with the pink circles.

Next, figure 4.7 presents a subtraction of the misfits (in absolute value) for the best value and zero value of the scaling factor for the velocities at the plate boundaries. For this model, we do not actually see much improvement, apart from some segments around the Cocos plate and Arabian plate. It does not provide us with much information at all. Probably adding the ridge-parallel resistance at the mid-ocean ridges actually has a larger effect on velocities further from the boundaries.

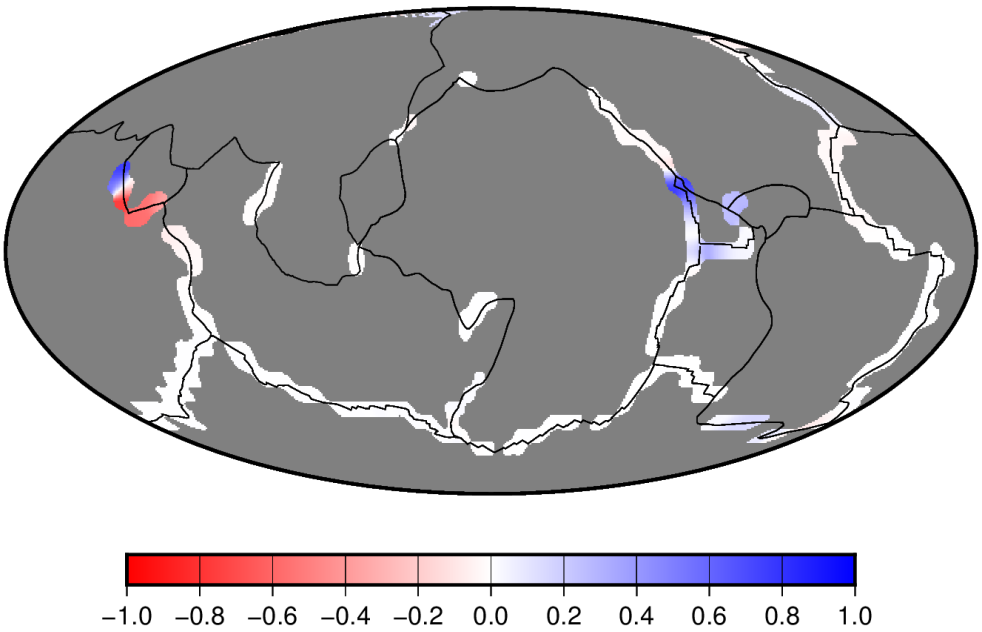

Figure 4.7: Subtraction plot of the misfits (in absolute value) for the best value $D_{rpr} = 4.71 \times 10^{11}\ N/m$ and zero value of the scaling factor for the velocities at the plate boundaries. The blue color indicate the areas where adding our force improves the previously used model, the red areas represent regions where the predictions are getting worse after adding the ridge-parallel resistance.

The predicted plate velocities compared to the observations using the best value of the scaling factor $4.71 \times 10^{11}\ N/m$ are shown in figure 4.8.

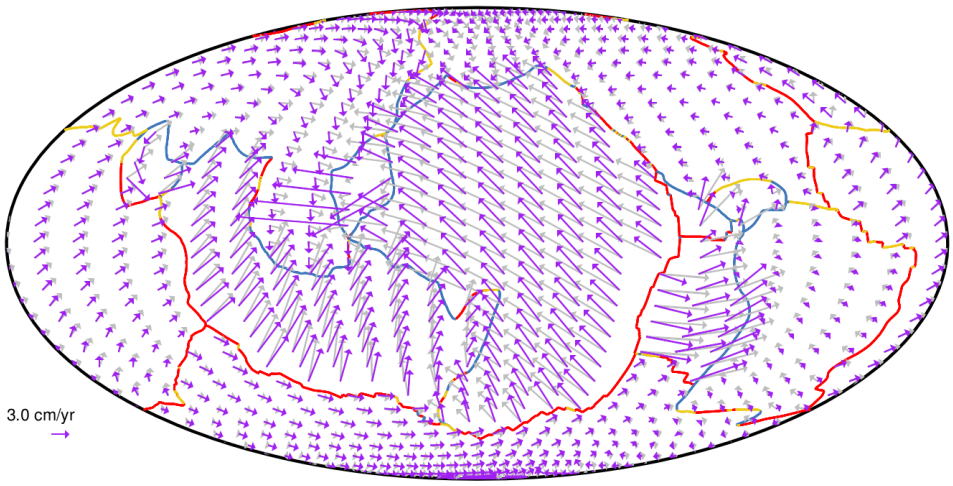

Figure 4.8: World map using the Mollweide projection, comparison of observed present-day plate motions (indicated by the grey arrows) with predicted plate motions (purple arrows) for $D_{rpr} = 4.71 \times 10^{11}\ N/m$. The average plate velocity for this model is 2.82 cm/yr.

Global map of a magnitude of the ridge-parallel resistance (see figure 4.9) for this model shows a pattern, which is basically the same as for the previous model (4.5), but the magnitude of the force is generally slightly lower, which is expected since the scaling factor for this model is a bit smaller (4.71×10^{11} vs. $6.28 \times 10^{11}\ N/m$ previously).

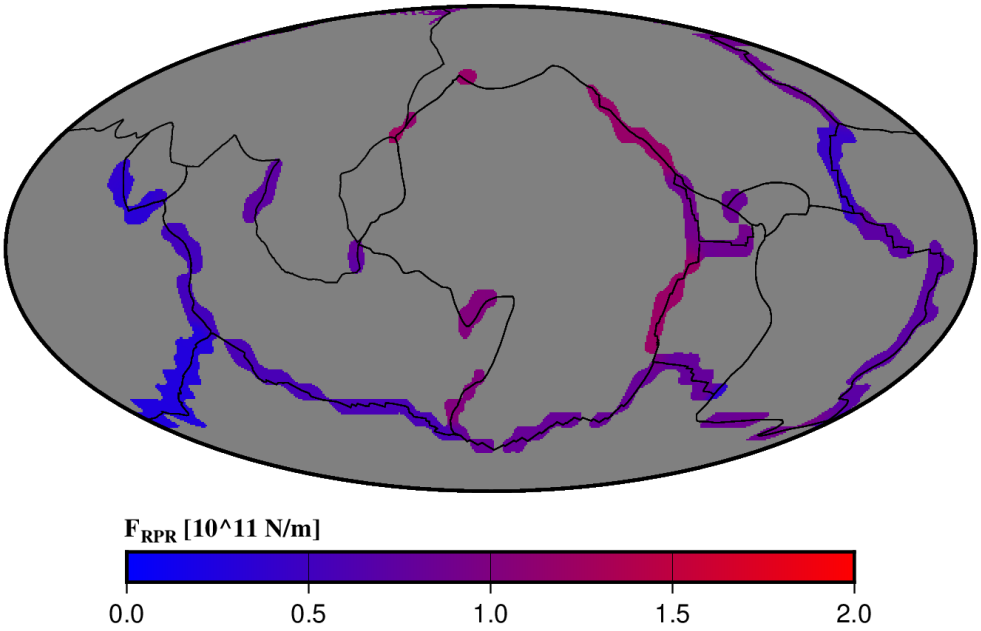

Figure 4.9: World map of a magnitude of the ridge-parallel resistance added to the torque balance at the mid-ocean ridges for $D_{rpr} = 4.71 \times 10^{11}\ N/m$.

4.3 Results evaluated by misfit in amplitude

4.3.1 Misfit in amplitude (whole Earth)

These results have been obtained using equation 3.7. In this case the best fit occurs when the misfit value is closest to 0. Figure 4.10 presents the misfit in amplitude over the whole surface of the globe. The best fit of 0.1458 was computed for a value of $12.56 \times 10^{11}\ N/m$ of D_{rpr} (the pink circle on the right). The misfit for a zero value of the scaling factor is 0.2108 (the pink circle on the left), thus the best fit was improved after adding the ridge-parallel resistance. Using this value of the factor, the average magnitude of the ridge-parallel resistance expressed as a stress at a certain segment of a plate boundary was calculated to 4.40 MPa.

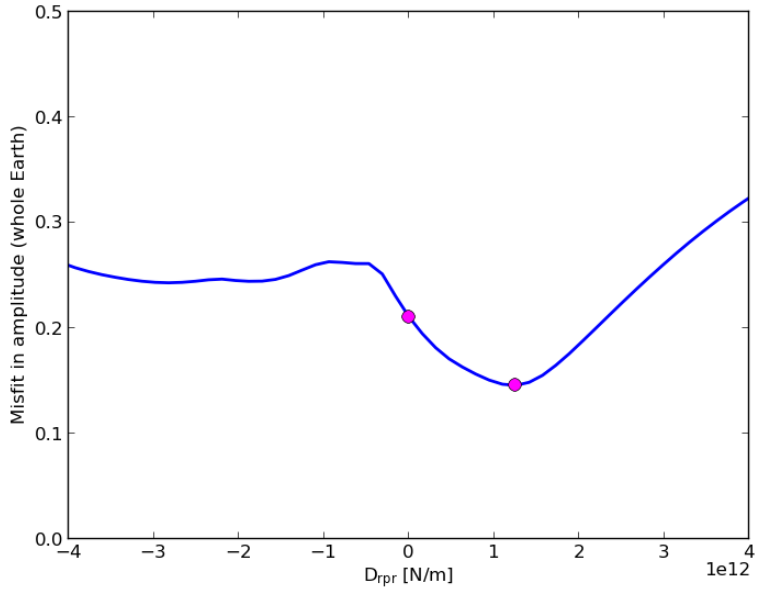

Figure 4.10: Misfit in amplitude over the whole surface of the globe. The best fit of 0.1458 for $D_{rpr} = 12.56 \times 10^{11}\ N/m$ and the misfit 0.2108 for a zero value of the scaling factor are marked with the pink circles.

Subtraction map 4.11 for this model shows that the improved/worsened areas are different from those for the model evaluated by misfit in direction (4.3). The improved predictions are now for the South American, African and Antarctic plates, as well as for large parts of the North American and Eurasian plates. The small plates (Arabian, Cocos and Caribbean plates) are now partially improved, partially worsened, and the predictions for the southern part of the North American plate are significantly worse than those of the previously used model Conrad and Lithgow-Bertelloni (2002, 2004).

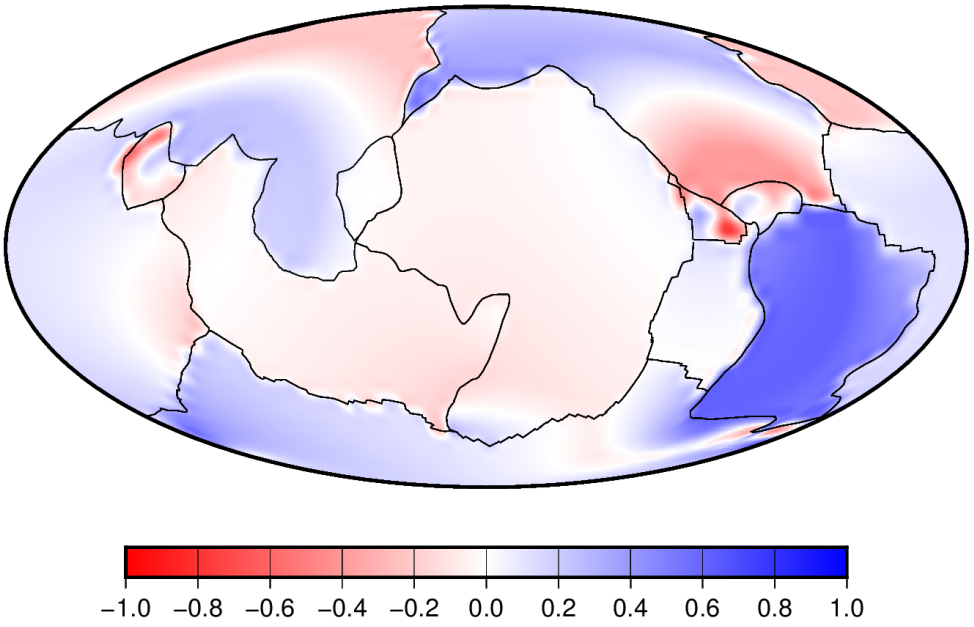

Figure 4.11: Subtraction plot of the misfits (in absolute value) for the best value $D_{rpr} = 12.56 \times 10^{11}\ N/m$ and zero value of the scaling factor for the velocities on the whole globe. The blue color indicates the areas where adding our force improves the previously used model, the red areas represent regions where the predictions are getting worse after adding the ridge-parallel resistance.

The predicted plate velocities compared to the observations using the best value of the scaling factor $12.56 \times 10^{11}\ N/m$ are shown in figure 4.12.

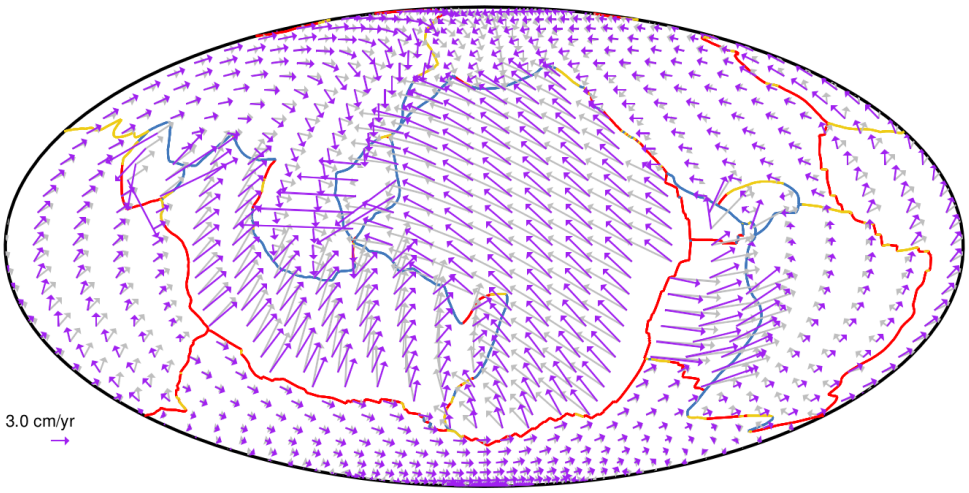

Figure 4.12: World map using the Mollweide projection, comparison of observed present-day plate motions (indicated by the grey arrows) with predicted plate motions (purple arrows) for $D_{rpr} = 12.56 \times 10^{11}\ N/m$. The average plate velocity for this model is 2.99 cm/yr.

Finally, figure 4.13 shows the global map of a magnitude of the ridge-parallel resistance. The pattern is again the same as for the previous global model (4.5), but the magnitude of the force now generally reaches higher values because the scaling factor for this model is higher.

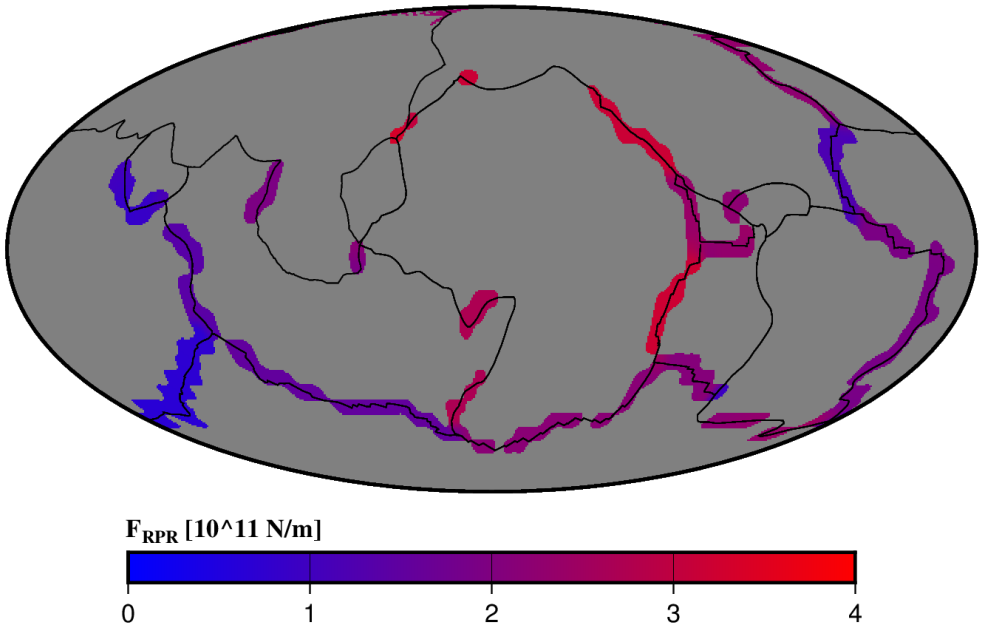

Figure 4.13: World map of a magnitude of the ridge-parallel resistance added to the torque balance at the mid-ocean ridges for $D_{rpr} = 12.56 \times 10^{11}\ N/m$. A different range of the scale had to be used in this case (compared to maps 4.5 and 4.9) due to the higher values of the force.

4.3.2 Misfit in amplitude (plate boundaries)

Figure 4.14 presents the misfit in amplitude at the plate boundaries. We again compare the best fit to the misfit for a zero value of the scaling factor D_{rpr}. The best fit of 0.1720 was computed for a value of $-1.57 \times 10^{11}\ N/m$ of D_{rpr} (the pink circle on the left). The misfit for a zero value of the scaling factor is 0.1801 (the pink circle on the right). The best fit was improved after adding the ridge-parallel resistance, but not by much. Using this value of the factor, the average magnitude of the ridge-parallel resistance expressed as a stress at a certain segment of a plate boundary was calculated to 5.5 MPa (assuming an average lithospheric thickness of 10 km at transform faults).

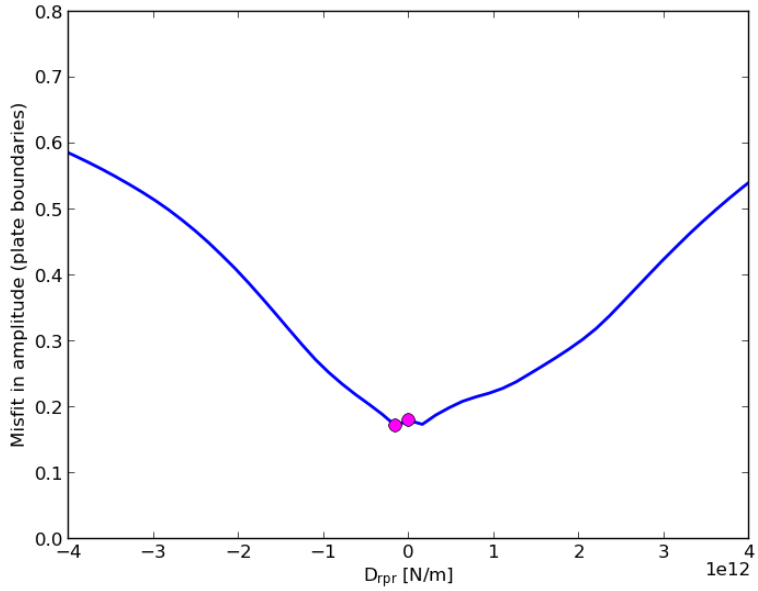

Figure 4.14: Misfit in amplitude at the plate boundaries. The best fit of 0.1720 for $D_{rpr} = -1.57 \times 10^{11}\ N/m$ and the misfit 0.1801 for a zero value of the scaling factor are marked with the pink circles.

Subtraction map 4.15 presents a subtraction of the misfits (in absolute value) for the best value and zero value of the scaling factor for the velocities at the plate boundaries. We see that for this model adding the ridge-parallel resistance does not improve the predictions directly at the plate boundaries either. The only blue segments are in the southern part of the Philippine plate. This is the only model, for which the value of the scaling factor is negative. The value is also very close to zero and does not provide us with much information, the map of predicted plate velocities compared to the observations is therefore not included.

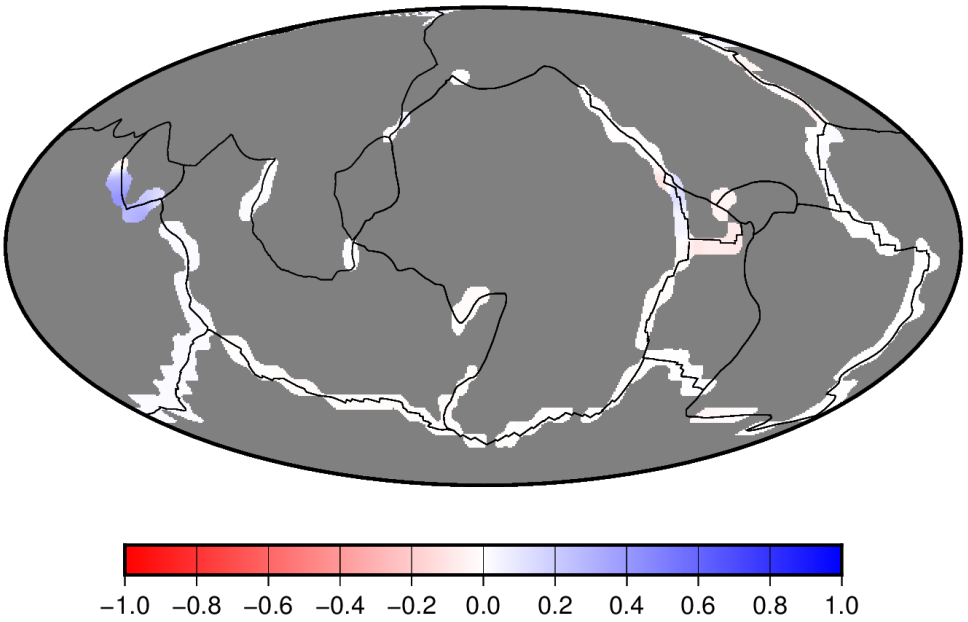

Figure 4.15: Subtraction plot of the misfits (in absolute value) for the best value $D_{rpr} = -1.57 \times 10^{11}\ N/m$ and zero value of the scaling factor for the velocities at the plate boundaries. The blue color indicate the areas where adding our force improves the previously used model, the red areas represent regions where the predictions are getting worse after adding the ridge-parallel resistance.

4.4 Results evaluated by misfit in direction and amplitude

4.4.1 Misfit in both direction and amplitude (whole Earth)

These results have been obtained using equation 3.8. The best fit occurs when the misfit value is again closest to 0. Figure 4.16 presents the misfit in both direction and amplitude over the whole surface of the globe. The best fit of 0.2720 was computed for a value of $4.71 \times 10^{11}\ N/m$ of D_{rpr} (the pink circle on the right). The misfit for a zero value of the scaling factor is 0.2973 (the pink circle on the left), thus the best fit was slightly improved after adding the ridge-parallel resistance. Using this value of the factor, the average magnitude of the ridge-parallel resistance expressed as a stress at a certain segment of a plate boundary was calculated to 16.5 MPa (assuming an average lithospheric thickness of 10 km at transform faults), which is the same result as we get for misfit in direction at the plate boundaries in section 4.2.2.

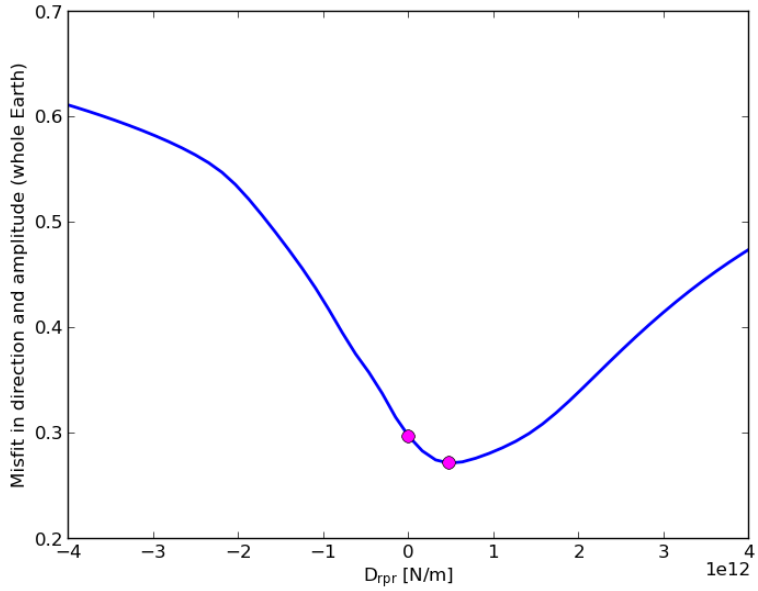

Figure 4.16: Misfit in both direction and amplitude over the whole surface of the globe. The best fit of 0.2720 for $D_{rpr} = 4.71 \times 10^{11}\ N/m$ and the misfit 0.2973 for a zero value of the scaling factor are marked with the pink circles.

The subtraction figure 4.17 for this model shows that the improved/worsened areas follow very similar pattern as those for the model evaluated by misfit in amplitude only (4.11). The improved predictions are again for the South American, African and Antarctic plates, as well as for large parts of the North American and Eurasian plates. The small plates (Arabian, Cocos and Caribbean plates) are again partially improved, partially worsened. The main difference is that in this case the predictions for the Pacific plate are slightly improved, whereas in the previous one they were slightly worse. The southern part of the North American plate shows deterioration for this model as well, but not as significant as previously. Overall, the contrast is not that high this time, which is caused by the lower value of the scaling factor.

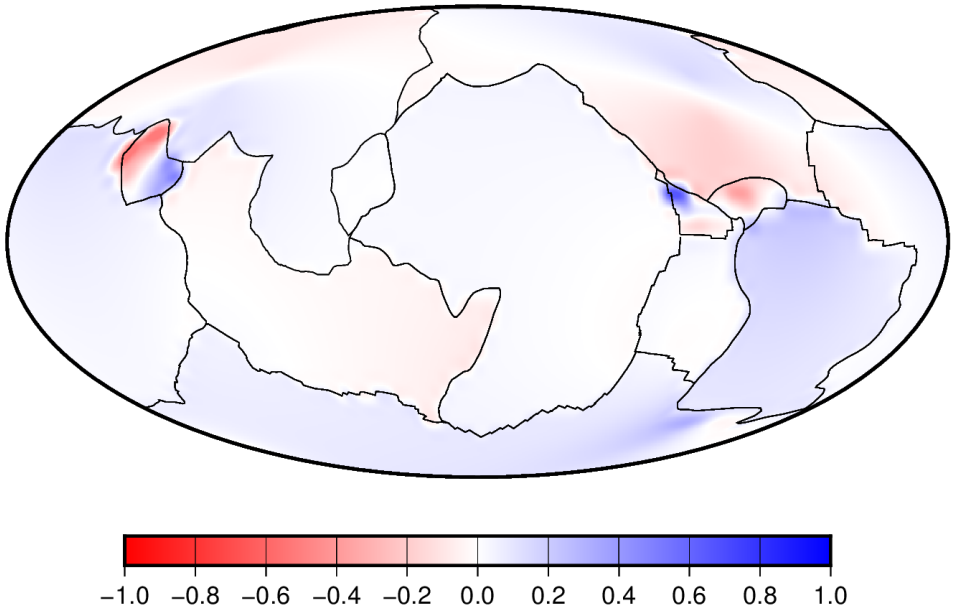

Figure 4.17: Subtraction plot of the misfits (in absolute value) for the best value $D_{rpr} = 4.71 \times 10^{11}\ N/m$ and zero value of the scaling factor for the velocities on the whole globe. The blue color indicates the areas where adding our force improves the previously used model, the red areas represent regions where the predictions are getting worse after adding the ridge-parallel resistance.

The predicted plate velocities compared to the observations using the best value of the scaling factor $4.71 \times 10^{11}\ N/m$ are shown in figure 4.18.

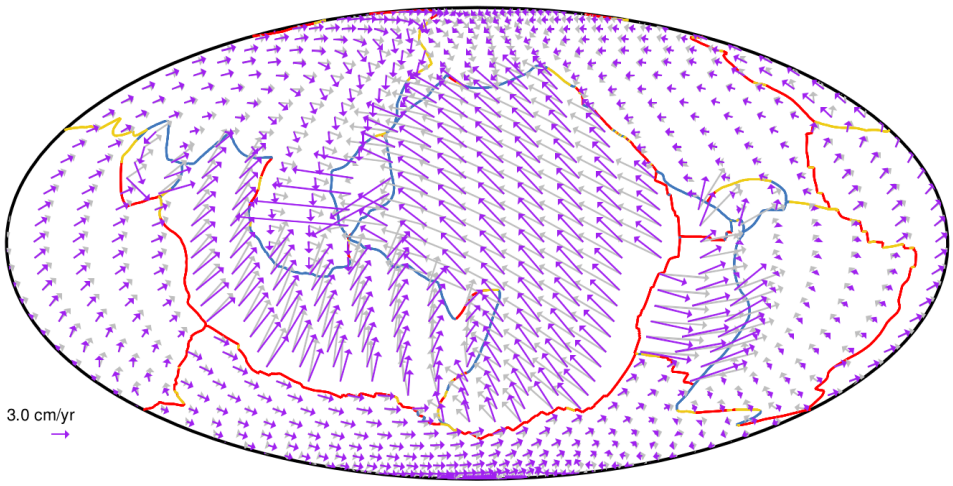

Figure 4.18: World map using the Mollweide projection, comparison of observed present-day plate motions (indicated by the grey arrows) with predicted plate motions (purple arrows) for $D_{rpr} = 4.71 \times 10^{11}\ N/m$. The average plate velocity for this model is 2.82 cm/yr.

When it comes to the magnitude of the actual force, it again follows the same pattern as the two previous global cases, only the values are now generally lower due to the lower value of the scaling factor D_{rpr}. The map would look exactly the same as figure 4.9 because the scaling factor has the same value in both cases, therefore I have not included it here.

4.4.2 Misfit in both direction and amplitude (plate boundaries)

Misfit function in both direction and amplitude for the plate boundaries (see figure 4.19) determines the best value of the scaling factor to $D_{rpr} = 3.14 \times 10^{11}\ N/m$ with the best fit of 0.3344. Using this value in our calculations, we get almost the same results as for misfit in direction for the plate boundaries (4.2.2), therefore I will not present these results here. The average magnitude of the ridge-parallel resistance expressed as a stress at a certain segment of a plate boundary is 11.0 MPa (assuming an average lithospheric thickness of 10 km at transform faults) for this model.

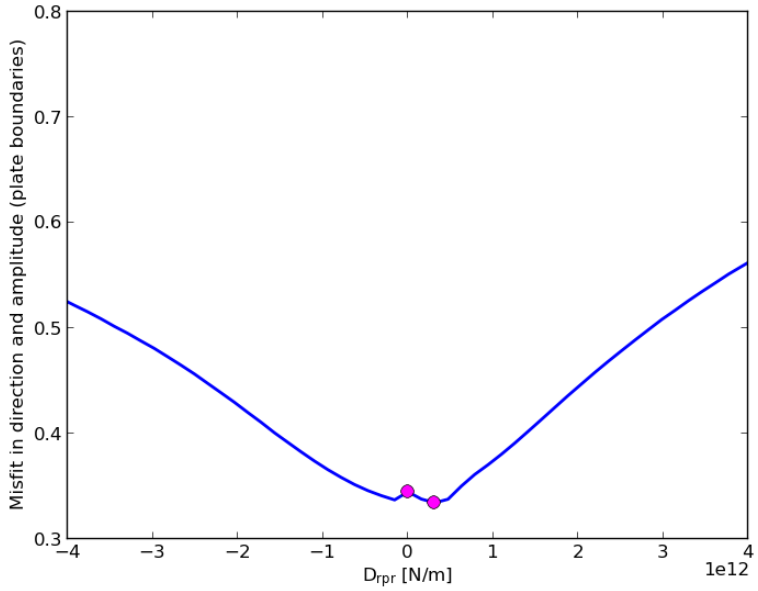

Figure 4.19: Misfit in both direction and amplitude at the plate boundaries. The best fit of 0.3344 for $D_{rpr} = 3.14 \times 10^{11}\ N/m$ and the misfit 0.3448 for a zero value of the scaling factor are marked with the pink circles.

Chapter 5

Discussion

The findings presented in the previous chapter have shown that the various misfit functions result in values of the scaling factor D_{rpr} that are not very different. All best fits show a slight improvement compared to the reference model Conrad and Lithgow-Bertelloni (2002, 2004). The three misfit functions calculated over the whole surface of the globe display improvements also when inspecting the subtraction maps, whereas the misfits computed only for the plate boundaries show almost no change in the predictions. This suggests that adding the ridge-parallel resistance at the mid-ocean ridges actually affects plate velocities further from the ridges more than those directly at the plate boundaries. Therefore, I will further focus mainly on the globally applied misfits functions.

Misfits in direction, amplitude, and both direction and amplitude together determine D_{rpr} values of 6.28×10^{11}, 12.56×10^{11} and 4.71×10^{11} N/m, respectively. Table 5.1 gives a short overview of the important numbers for each of the evaluated global models, including the stress corresponding to the value of the scaling factor used. We assume an average lithospheric thickness of 10 km at transform faults, where the force usually has the maximum effect due to typically shorter lengths along the transform faults. In addition, an average value of F_{rpr} for each model can be found in table 5.1. The force is computed using equation 3.2 and the resulting range is between 0.8 and 2.1×10^{11} N/m. We see that in terms of the best fit, misfit in amplitude shows the best improvement compared to the zero value (the second column in table 5.1 represents the difference between the best fit for the reference model and our computed best fit; the highest number means the biggest improvement). However, when we look at the subtraction maps (figures 4.3, 4.11 and 4.17), the largest improved (blue) area is displayed for

Misfit function	Best fit improved	Average $\mathbf{D_{rpr}}$[N/m]	Average $\mathbf{F_{rpr}}$[N/m]	Average $\sigma_{\mathbf{rpr}}$[MPa]
misfit in direction	0.0074	6.28×10^{11}	1.04×10^{11}	22.0
misfit in amplitude	0.0650	12.56×10^{11}	2.07×10^{11}	44.0
misfit in both	0.0252	4.71×10^{11}	0.78×10^{11}	16.5

Table 5.1: Short overview of the important numbers for each of the evaluated global models. The columns represent: type of the misfit function used, the difference between the best fit for the reference model and our computed best fit, the scaling factor, the average magnitude of our force and the corresponding average stress.

the misfit in both direction and amplitude together. The misfit in amplitude shows more improvement for the improved areas (the blue areas are more blue). On the other hand, the worsened regions are much worse. Generally, in this case the contrast is much higher than for the other models. Although the computed scaling factors are not very different, the subtraction maps display some significant differences in their predictions.

In this study, we expected to improve the inconsistencies between the reference model of predicted plate motions (Conrad and Lithgow-Bertelloni, 2002, 2004) and the observations particularly for the plates surrounded mostly by mid-oceanic ridges. But by inspecting the three subtraction maps, it is obvious that that is not always the case. For example, the Pacific, Nazca and Cocos plates were expected to improve. Although the Pacific plate is slightly blue on the maps for misfit in direction and misfit in both, the third model indicates worsened prediction for this plate. The Cocos plate is partially improved and partially worsened on all three maps. On the contrary, the Nazca plate is almost unaffected by our calculations. Only misfit in amplitude displays a very subtle improvement for this plate. The fact that the blue areas are not always associated with the mid-ocean ridges can be explained by the nature of the motion of the plates that are all connected and interact with each other. The added torque causes recalculations of the rotation poles and influence all the plates. This happens through the mantle flow; a change to the direction of one plate affects mantle flow, which affects all the other plates.

To determine the relative importance of our force, I compare its magnitude to the other major forces associated with plate tectonics. The diagram below (figure 5.1) presents their ranges of estimates. The estimated magnitude of the ridge-parallel resistance F_{rpr} between 0.8 and 2.1×10^{11} N/m (assuming an average length of a segment around 90 km) is not unreasonable compared to the magnitude of the slab pull forces being around 1 to 5×10^{13} N/m depending on the properties of the considered slab

(Wu et al., 2008). We expected our force to be weaker, since slab pull is the main driving force acting on plates. Another major plate-driving force, the ridge push, has been estimated from 3.4×10^{12} to 3.9×10^{12} N/m in Turcotte and Schubert (2014) (equilibrated ocean basin vs. total ridge push on 100 Myr old oceanic lithosphere). This force is less important than slab pull, but it is still one of the major forces associated with plate tectonics, so a higher number than we found for F_{rpr} is not surprising.

The final estimate of our force expressed as a stress is comparable to the shear tractions that mantle flow exerts on the base of lithosphere and which also contribute to plate-driving forces. They are calculated to reach from 2 to 5 MPa (Conrad and Lithgow-Bertelloni, 2006) or 2×10^{12} N/m to 5×10^{13} N/m depending on the length of a plate (I used 10 000 km for the Pacific plate and 1 500 km for the Cocos plate (Conrad and Hager, 1999)). This big range is caused by the large variation in sizes of plates. Our estimates of the stress between 16.5 and 44.0 MPa (assuming an average lithospheric thickness of 10 km at transform faults) may seem too high when comparing to these basal stresses, but the fact that in our case the stresses act only at plate boundaries and have therefore smaller influence, whereas basal shear tractions are spread over large areas (the whole plates), could explain our high number. Our values represent the average stress for the corresponding models. From the three maps showing the magnitude of F_{rpr} force along the plate boundaries (figures 4.5, 4.9 and 4.13), we can interpret the relative strength of the associated stress and see that the values are mostly in the lower part of the displayed range (especially on the first two maps).

As mentioned above, the new force should usually have the maximum effect at transform faults due to commonly shorter lengths along this type of plate boundaries. When comparing the total length of oceanic spreading ridges vs. oceanic transform faults, the obtained values are 67 000 km and 48 000 km, respectively (Bird, 2003), which means that the magnitude of the resistance should be typically around 1.4 times higher at the faults compared to ridges. There we should actually talk about transform-perpendicular resistance. The estimated magnitude of this transform-perpendicular resistive force is between 1.1 and 2.9×10^{11} N/m.

The final comparison of changes caused by including our F_{rpr} in the force balance is displayed in the figure 5.2. Here we see the predictions done by our best model with $D_{rpr} = 4.71 \times 10^{11}\ N/m$ compared to the reference model. For most of the plates, the changes are very subtle. Exceptions are the small plates that actually exhibit some

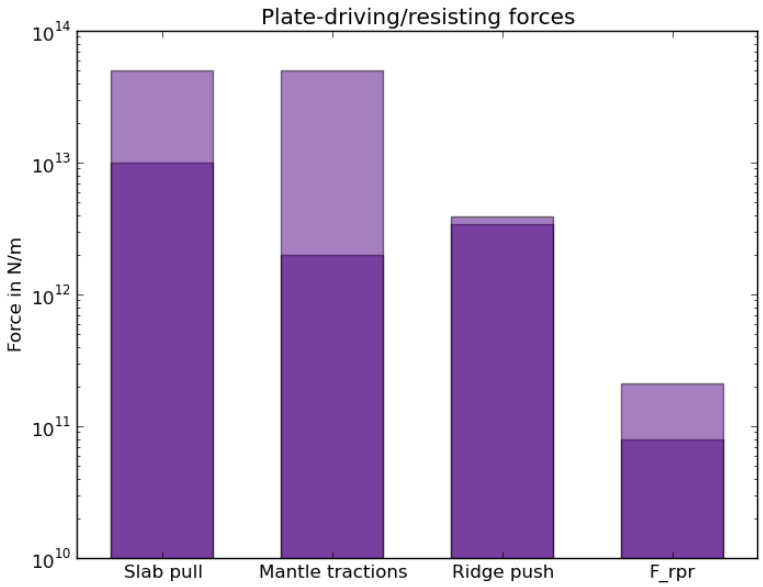

Figure 5.1: Comparison between the expected magnitudes of the various plate-driving/resisting forces: slab pull, mantle tractions, ridge push, and our ridge-parallel resistance F_{rpr}; displayed with their range of estimates in N/m. The estimated magnitude of the ridge-parallel resistance F_{rpr} is between 0.8 and 2.1×10^{11} N/m (assuming an average length of a segment around 90 km), the magnitude of the slab pull forces around 1 to 5×10^{13} N/m depending on the properties of the considered slab (Wu et al., 2008). The ridge push has been estimated from 3.4×10^{12} to 3.9×10^{12} N/m in Turcotte and Schubert (2014) (equilibrated ocean basin vs. total ridge push on 100 Myr old oceanic lithosphere), and the mantle tractions are calculated to reach from 2 to 5 MPa (Conrad and Lithgow-Bertelloni, 2006) or 2×10^{12} N/m to 5×10^{13} N/m depending on the length of a plate (I used 10 000 km for the Pacific plate and 1 500 km for the Cocos plate (Conrad and Hager, 1999)).

variations. For example, the Arabian plate gets significantly twisted partially clockwise, partially counterclockwise, which could be explained by our force making the difference of the ridge-parallel components smaller. Unfortunately, it improves the predictions for only half of the plate (see figure 4.17). A similar situation is shown for the Cocos plate, which has two parts of boundaries with ridges that are perpendicular to each other and by forcing the vectors to get more normal to one of them, the one half of the plate gets better but the other one gets actually worse. Most of the large plates are slightly improved, but the changes are not obvious.

At the end, I briefly discuss the questions associated with our study that could be addressed in future research. Firstly, as described in section 3.3, we used a limit value of -0,5 cm/yr to identify the mid-ocean ridges. Since the resolution was still not good

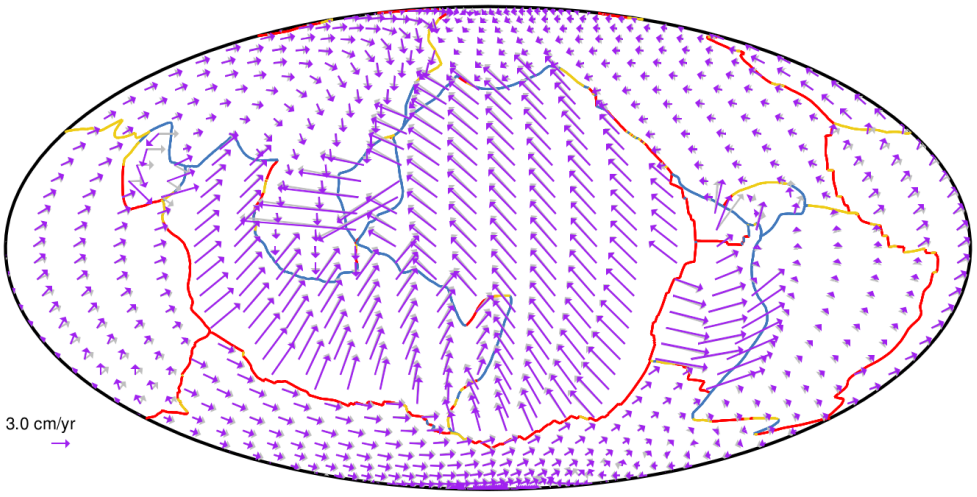

Figure 5.2: World map using the Mollweide projection, comparison of the reference model of plate motions (indicated by the grey arrows) with predicted plate motions (purple arrows) for $D_{rpr} = 4.71 \times 10^{11}\ N/m$ evaluated by misfit in both direction and amplitude together. The average plate velocity for this model is 2.82 cm/yr.

enough to exclude all the transform faults from our selection of segments, it is basically certain that we have added the ridge-parallel resistance to some segments that are actually transform faults. Including our force to a transform fault would not improve the predictions for that segment, because F_{rpr} acts in a direction parallel to a segment and for transform faults the perpendicular movement is the unwanted component. Therefore, to repeat this study again with an updated high-resolution plate motion model, which would include transform faults (and probably a higher number of plates), could be useful. It might allow us to actually measure the transform-perpendicular force.

Secondly, plate velocities depend on viscosity, therefore assumptions about the viscosity profile should affect the predictions significantly. We have not considered the influence of different viscosity values on the ridge-parallel resistance, but it could be interesting to investigate this aspect of its behavior as well. I assume that testing of different layered homogeneous viscosity structures would not affect the pattern of our force significantly, since it would probably influence all the ridges in the same way, but lateral viscosity variations could be responsible for more important changes in the predictions (van Summeren et al., 2012).

Chapter 6

Conclusion

In this study, we have demonstrated that including the ridge-parallel resistance in the force balance using the torque balance approach slightly improves the predictions of plate motions. All misfit functions used to evaluate our results have shown improvement in the values of the best fit and the three global misfit functions even displayed better predictions of the plate motions compared to the reference model. Overall, relative to the reference model, the greatest improvement is apparent in the model evaluated by the misfit in both direction and amplitude together with the average value of $F_{rpr} = 0.78 \times 10^{11}\ N/m$. The improved areas include the Pacific, South American, African and Antarctic plates, as well as large parts of the North American and Eurasian plates. The small plates (Arabian, Cocos and Caribbean plates) are partially improved, partially worsened. The predictions for the rest of the plates are worse, but not significantly.

We have also managed to estimate the magnitude of the new force and show that it has a relatively small contribution to the global plate motions compared to the major forces. Our estimates of the ridge-parallel resistance expressed as a stress are in a range between 16.5 and 44.0 MPa (assuming an average lithospheric thickness of 10 km at transform faults), which is an order of magnitude smaller than an estimate for ridge push force and two orders of magnitude smaller than the expected values of the slab pull and basal tractions. When expressed as an actual force, the magnitude of the ridge-parallel resistance is in a range from 0.8 to 2.1×10^{11} N/m at mid-ocean ridges, or between 1.1 and 2.9×10^{11} N/m at transform faults (transform-perpendicular resistance).

These results are the first constraint on this force using plate motions, which highlights the importance of our project. The small amplitude compared to the other plate forces suggests that ridge-parallel resistance or transform-perpendicular resistance is either a small amplitude force with little impact on plate motions, or the plate motions have adjusted to minimize the resistive force.

Bibliography

Argus, D. F. and Heflin, M. B. (1995). Plate motion and crustal deformation estimated with geodetic data from the global positioning system. *Geophysical Research Letters*, 22(15):1973–1976.

Ballmer, M. D., Schmerr, N. C., Nakagawa, T., and Ritsema, J. (2015). Compositional mantle layering revealed by slab stagnation at ∼1000-km depth. *Science advances*, 1(11):e1500815.

Becker, T. W. and O'Connell, R. J. (2001). Predicting plate velocities with mantle circulation models. *Geochemistry, Geophysics, Geosystems*, 2(12).

Bird, P. (2003). An updated digital model of plate boundaries. *Geochemistry, Geophysics, Geosystems*, 4(3).

Chapple, W. M. and Tullis, T. E. (1977). Evaluation of the forces that drive the plates. *Journal of geophysical research*, 82(14):1967–1984.

Conrad, C. P., Bilek, S., and Lithgow-Bertelloni, C. (2004). Great earthquakes and slab pull: interaction between seismic coupling and plate–slab coupling. *Earth and Planetary Science Letters*, 218(1-2):109–122.

Conrad, C. P. and Hager, B. H. (1999). Effects of plate bending and fault strength at subduction zones on plate dynamics. *Journal of Geophysical Research: Solid Earth*, 104(B8):17551–17571.

Conrad, C. P. and Lithgow-Bertelloni, C. (2002). How mantle slabs drive plate tectonics. *Science*, 298(5591):207–209.

Conrad, C. P. and Lithgow-Bertelloni, C. (2004). The temporal evolution of plate driving forces: Importance of "slab suction" versus "slab pull" during the cenozoic. *Journal of Geophysical Research: Solid Earth*, 109(B10).

Conrad, C. P. and Lithgow-Bertelloni, C. (2006). Influence of continental roots and asthenosphere on plate-mantle coupling. *Geophysical Research Letters*, 33(5).

Davies, G. F. (1988). Ocean bathymetry and mantle convection: 1. Large-scale flow and hotspots. *Journal of Geophysical Research: Solid Earth*, 93(B9):10467–10480.

Elsasser, W. M. (1969). Convection and stress propagation in the upper mantle. *The Application of Modern Physics to the Earth and Planetary Interiors*, pages 223–246, edited by S. K. Runcorn.

Forsyth, D. and Uyeda, S. (1975). On the relative importance of the driving forces of plate motion. *Geophysical Journal International*, 43(1):163–200.

Glazner, A. F. (1991). Plutonism, oblique subduction, and continental growth: An example from the mesozoic of California. *Geology*, 19(8):784–786.

Gordon, R. G., Cox, A., and Harter, C. E. (1978). Absolute motion of an individual plate estimated from its ridge and trench boundaries. *Nature*, 274(5673):752.

Hager, B. H. (1984). Subducted slabs and the geoid: Constraints on mantle rheology and flow. *Journal of Geophysical Research: Solid Earth*, 89(B7):6003–6015.

Hager, B. H. and O'Connell, R. J. (1981). A simple global model of plate dynamics and mantle convection. *Journal of Geophysical Research: Solid Earth*, 86(B6):4843–4867.

Hall, C. E., Gurnis, M., Sdrolias, M., Lavier, L. L., and Müller, R. D. (2003). Catastrophic initiation of subduction following forced convergence across fracture zones. *Earth and Planetary Science Letters*, 212(1-2):15–30.

Kozák, J. and Čermák, V. (2010). *The illustrated history of natural disasters*. Springer.

Kreemer, C., Holt, W. E., and Haines, A. J. (2003). An integrated global model of present-day plate motions and plate boundary deformation. *Geophysical Journal International*, 154(1):8–34.

Lithgow-Bertelloni, C. and Richards, M. A. (1998). The dynamics of cenozoic and mesozoic plate motions. *Reviews of Geophysics*, 36(1):27–78.

McKenzie, D. P. (1969). Speculations on the consequences and causes of plate motions. *Geophysical Journal International*, 18(1):1–32.

Müller, R. D., Sdrolias, M., Gaina, C., and Roest, W. R. (2008). Age, spreading rates, and spreading asymmetry of the world's ocean crust. *Geochemistry, Geophysics, Geosystems*, 9(4).

Ricard, Y. and Vigny, C. (1989). Mantle dynamics with induced plate tectonics. *Journal of Geophysical Research: Solid Earth*, 94(B12):17543–17559.

Richards, M. A. and Lithgow-Bertelloni, C. (1996). Plate motion changes, the Hawaiian-Emperor bend, and the apparent success and failure of geodynamic models. *Earth and Planetary Science Letters*, 137(1-4):19–27.

Richardson, R. M. (1992). Ridge forces, absolute plate motions, and the intraplate stress field. *Journal of Geophysical Research: Solid Earth*, 97(B8):11739–11748.

Richardson, R. M., Solomon, S. C., and Sleep, N. H. (1979). Tectonic stress in the plates. *Reviews of Geophysics*, 17(5):981–1019.

Richter, F. M. (1975). On the driving mechanism of plate tectonics. *Tectonophysics*, 38:61–88.

Ryan, W. B. F., Carbotte, S. M., Coplan, J. O., O'Hara, S., Melkonian, A., Arko, R., Weissel, R. A., Ferrini, V., Goodwillie, A., Nitsche, F., Bonczkowski, J., and Zemsky, R. (2009). Global multi-resolution topography synthesis. *Geochemistry, Geophysics, Geosystems*, 10(3).

Sleep, N. H. (1990). Hotspots and mantle plumes: Some phenomenology. *Journal of Geophysical Research: Solid Earth*, 95(B5):6715–6736.

Smoczyk, G., Hayes, G., Hamburger, M., Benz, H., Villasenor, A., and Furlong, K. (2010). Seismicity of the earth 1900-2012: Philippine sea plate and vicinity, USGS open-file report 2010-1083.

Solomon, S. C. and Sleep, N. H. (1974). Some simple physical models for absolute plate motions. *Journal of Geophysical Research*, 79(17):2557–2567.

Solomon, S. C., Sleep, N. H., and Richardson, R. M. (1975). On the forces driving plate tectonics: Inferences from absolute plate velocities and intraplate stress. *Geophysical Journal International*, 42(2):769–801.

Steiner, S. A. and Conrad, C. P. (2007). Does active mantle upwelling help drive plate motions? *Physics of the Earth and Planetary Interiors*, 161(1-2):103–114.

Tackley, P. J. (2000). Self-consistent generation of tectonic plates in time-dependent, three-dimensional mantle convection simulations. *Geochemistry, Geophysics, Geosystems*, 1(8).

Turcotte, D. and Oxburgh, E. (1967). Finite amplitude convective cells and continental drift. *Journal of Fluid Mechanics*, 28(1):29–42.

Turcotte, D. and Schubert, G. (2014). *Geodynamics*. Cambridge university press.

Van Kranendonk, M. J. (2011). Onset of plate tectonics. *Science*, 333(6041):413–414.

van Summeren, J., Conrad, C. P., and Lithgow-Bertelloni, C. (2012). The importance of slab pull and a global asthenosphere to plate motions. *Geochemistry, Geophysics, Geosystems*, 13(2).

Wei, M. (2017). What transform faults in the ocean can tell us. *Research features*.

Wu, B., Conrad, C. P., Heuret, A., Lithgow-Bertelloni, C., and Lallemand, S. (2008). Reconciling strong slab pull and weak plate bending: The plate motion constraint on the strength of mantle slabs. *Earth and Planetary Science Letters*, 272(1-2):412–421.